Article

Cell

Alzheimer's disease patient-derived high-molecular-weight tau impairs bursting in hippocampal neurons

Graphical abstract

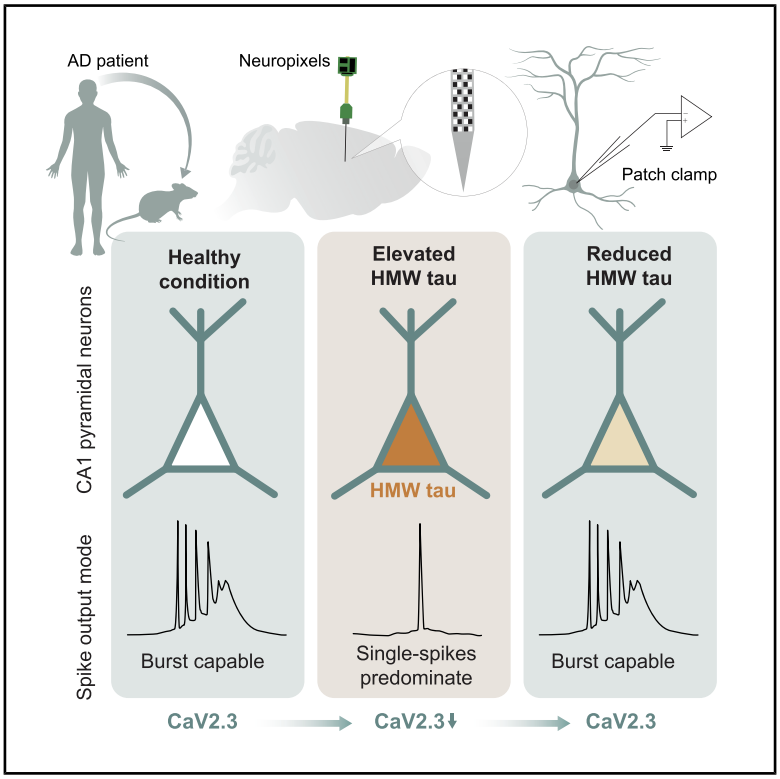

Authors

Samuel S. Harris, Robert Ellingford, Jana Hartmann, ..., Andreas Neef, Bradley T. Hyman, Marc Aurel Busche

Correspondence

samuel.harris@ucl.ac.uk (S.S.H.), m.busche@ucl.ac.uk (M.A.B.)

In brief

In mouse models, tau impairs neuronal complex spike bursting and associated network processes in hippocampus CA1 alongside CaV2.3 downregulation. Soluble high-molecular-weight tau species drive these impairments, as lowering levels rectifies deficits and AD patient-derived extracts selectively compromise burst generation.

Highlights

- Tau pathology in mice is associated with reduced bursting in CA1 excitatory neurons
- Bursting deficits relate to neuronal CaV2.3 downregulation and network dysfunction
- Suppressing soluble tau rectifies CaV2.3 expression and fast complex bursting
- Human AD HMW tau species selectively impair bursting at nanomolar concentrations

Harris et al., 2025, Cell *188*, 3775–3788
July 10, 2025
https://doi.org/10.1016/j.cell.2025.04.006

CellPress

Cell

CellPress
OPEN ACCESS

Article

Alzheimer's disease patient-derived high-molecular-weight tau impairs bursting in hippocampal neurons

Samuel S. Harris,[1,*] Robert Ellingford,[1,11] Jana Hartmann,[1,11] Debanjan Dasgupta,[1,11,12] Marten Kehring,[1] Rikesh M. Rajani,[1,2] David Graykowski,[1] Noé Quittot,[3] Dhanush Sivasankaran,[3] Caitlin Commins,[3] Zhanyun Fan,[3] Suraya A. Bond,[1] Fred Wolf,[4] David Dupret,[5] Raymond J. Dolan,[6] Arthur Konnerth,[7,8] Andreas Neef,[4] Bradley T. Hyman,[3] and Marc Aurel Busche[1,9,10,13,*]

[1]UK Dementia Research Institute at University College London, London, UK
[2]British Heart Foundation - UK Dementia Research Institute Centre for Vascular Dementia Research at The University of Edinburgh, Edinburgh, UK
[3]Department of Neurology, Massachusetts General Hospital, Harvard Medical School, Charlestown, MA, USA
[4]Göttingen Campus Institute for Dynamics of Biological Networks, Göttingen, Germany
[5]Medical Research Council Brain Network Dynamics Unit, Nuffield Department of Clinical Neurosciences, University of Oxford, Oxford, UK
[6]Max Planck UCL Centre for Computational Psychiatry and Ageing Research, London, UK
[7]Institute of Neuroscience, Technical University of Munich, Munich, Germany
[8]Munich Cluster for Systems Neurology (SyNergy), Munich, Germany
[9]Department of Neurodegenerative Diseases, University Hospital of Geriatric Medicine FELIX PLATTER and University of Basel, Basel, Switzerland
[10]Department of Biomedicine, University of Basel, Basel, Switzerland
[11]These authors contributed equally
[12]Present address: Department of Biological Sciences and Bioengineering (BSBE) & MFCEM, Indian Institute of Technology, Kanpur, India
[13]Lead contact
*Correspondence: samuel.harris@ucl.ac.uk (S.S.H.), m.busche@ucl.ac.uk (M.A.B.)
https://doi.org/10.1016/j.cell.2025.04.006

SUMMARY

Tau accumulation is closely related to cognitive symptoms in Alzheimer's disease (AD). However, the cellular drivers of tau-dependent decline of memory-based cognition remain elusive. Here, we employed *in vivo* Neuropixels and patch-clamp recordings in mouse models and demonstrate that tau, independent of β-amyloid, selectively debilitates complex-spike burst firing of CA1 hippocampal neurons, a fundamental cellular mechanism underpinning learning and memory. Impaired bursting was associated with altered hippocampal network activities that are coupled to burst firing patterns (i.e., theta rhythms and high-frequency ripples) and was concurrent with reduced neuronal expression of CaV2.3 calcium channels, which are essential for burst firing *in vivo*. We subsequently identify soluble high molecular weight (HMW) tau, isolated from human AD brain, as the tau species responsible for suppression of burst firing. These data provide a cellular mechanism for tau-dependent cognitive decline in AD and implicate a rare species of intracellular HMW tau as a therapeutic target.

INTRODUCTION

Alzheimer's disease (AD) is characterized by the presence of β-amyloid (Aβ) plaques and tau neurofibrillary tangles (NFTs) in patient brains, but it is the burden, spatial extent, and region-specificity of tau pathology that are most closely related to disease-related cognitive impairment. Recent evidence suggests that soluble tau, rather than tangles, most strongly correlates to patients' clinical progression rate.[1,2] Similarly, in mouse models, interventions that suppress soluble tau have been shown to restore network and memory function,[3,4] suggesting that soluble tau actively impairs neuronal function critical for learning and memory. Nevertheless, the underlying mechanism for this impairment remains unknown.

Hippocampal pyramidal neurons transmit information via individual action potentials (spikes) and complex spike bursts. Bursts are cellular-level events comprising 2–6 consecutive spikes, typically decreasing in amplitude and separated by brief inter-spike intervals (ISIs, <10 ms).[5–7] Burst firing enhances the reliability of information transfer, improves informational content, and is linked to activity-dependent synaptic plasticity, which can support memory-guided behavior.[8–11] Indeed, learning has been shown to enhance burst firing in the cortex and hippocampus,[12–14] and burst firing is sufficient for learning

hippocampus-dependent tasks.[15] Burst firing is also critical for behavioral timescale synaptic plasticity (BTSP) underpinning the formation and remapping of hippocampal place fields, and it is essential for the formation of cognitive maps and representations of episodic and spatial memories, which tend to arise in neurons with a high intrinsic propensity for bursting.[16–18] Correspondingly, at the network level, neuronal bursting in the hippocampus supports theta-rhythmic computations during spatial navigation and memory,[6] and it is also a feature of offline neuronal replay (i.e., sequential reactivation of neuronal ensembles representing prior experiences) during sharp wave ripples, highly synchronous population patterns that are critical to memory consolidation and other cognitive operations including decision-making and inference.[19,20] These findings highlight bursting as a fundamental cellular-level neurophysiological mechanism that is central to memory and cognition.

Accordingly, here, we tested the hypothesis that AD-related pathology, in particular specific species of soluble human tau, deleteriously impacts neuronal burst spiking in hippocampus CA1, a site of early tau pathology accumulation in AD, which foreshadows cognitive decline. Using *in vivo* high-density Neuropixels and patch-clamp recordings in AD mouse models, we reveal that tau, whether or not concurrent with Aβ pathology, markedly and selectively debilitates neuronal bursting, but not single-spike firing, in CA1 hippocampus and impacts negatively on local circuit-level processes that support learning and memory and critically rely on burst firing. We go on to show that tau-dependent impaired bursting is associated with reduced neuronal expression of CaV2.3 calcium channels that underpin this high-frequency spike output mode *in vivo*, and we identify a rare species of soluble high molecular weight (HMW) tau, isolated directly from the human AD brain and also present in our mouse models, as the principal instigator of abnormal burst firing in CA1 hippocampal neurons at (patho)physiologically relevant nanomolar concentrations. These findings thus provide a candidate cellular mechanism linking tau-associated cognitive deficits to a specific neuronal dysfunction.

RESULTS

AD pathology impairs neuronal bursting in hippocampal neurons during spontaneous awake behaviors and internally evoked population events

We first examined neuronal bursting in the hippocampus during spontaneous behaviors in awake head-fixed 9-month-old APP/PS1-rTg4510 mice accumulating both Aβ and tau pathology,[21] akin to humans with AD, relative to age-matched wild-type (WT) littermate controls. We implanted high-density Neuropixels probes into CA1 and computationally spike-sorted and extracted action potential firing events from putative excitatory pyramidal neurons, based on waveform dynamics (Figures 1A–1C and S1A). Assessment of the probability distribution of inter-spike intervals (ISIs) of putative excitatory pyramidal neurons across behavioral states (including awake resting and locomotion) revealed a maximum between 2 and 6 ms, corresponding to an intra-burst ISI peak,[5,22] visibly prominent in neurons from WT controls but markedly absent in neurons from APP/PS1-rTg4510 animals (Figure 2A). This effect was manifested at the single animal level by a significant increase in modal ISI (i.e., the most frequent ISI, averaged across neurons for each animal) in APP/PS1-rTg4510 mice versus WTs (Figure 2B). To quantify and compare the propensity for neurons to discharge bursts between genotypes, we computed a burst index (proportion of ISIs < 10 ms[5,6,13,23]; threshold indicated as gray line in Figure 2A). This showed a significant reduction in bursting during both resting and locomotion states in APP/PS1-rTg4510 animals relative to WTs (Figure 2C). Notably, the "burstiness" (i.e., burst index) of neurons across genotypes remained stable over different behaviors, with a slight trend toward increased bursting during resting states, consistent with earlier findings (Figure 2D).[5]

Alongside the marked debilitation of neuronal bursting, we also observed a reduction in resting-state neuronal firing rates in APP/PS1-rTg4510 mice relative to WTs (Figure 2E), in line with previous two-photon calcium imaging results (serving as a proxy for neuronal firing) ascribed to the effects of tau pathology.[3,24] To examine the impact of compromised neuronal bursting on this hypoactivity phenotype, we next dissected resting-state neuronal firing rates by the contribution of single spikes and burst spikes. We found only burst spike rates, but not single-spike rates, to be significantly reduced in APP/PS1-rTg4510 mice versus WTs (Figure 2F). This effect, importantly, remained undiminished after accounting for differences in resting-state neuronal firing rates and inter-animal variability across genotypes, using a linear mixed-effects model (Figure 2G). Moreover, simple linear modeling of the contribution of burst spikes to overall neuronal firing rates (i.e., the sum of both single and burst spiking) enabled a close prediction of the marked neuronal hypoactivity phenotype observed in APP/PS1-rTg4510 mice relative to WTs (~60% fall, Figures 2H and S1B). These findings suggest that neuronal hypoactivity in APP/PS1-rTg4510 mice is primarily driven by a reduction in burst firing, rather than by changes in single-spike activity, and point toward an AD pathology-dependent, but behavioral-state-independent, impairment of neuronal bursting *in vivo*.

To examine whether neuronal bursting impairments during spontaneous awake behaviors also extended to deficits during intrinsically evoked population events, we identified high-frequency oscillatory ripples in CA1. Ripples are prominent during offline/resting states and play a key role in the offline consolidation of memory traces[25] and hippocampal cell assemblies[26] and are associated with pronounced burst firing[20] (Figure S1C). Notably, we found that the incidence of ripple events was significantly reduced in APP/PS1-rTg4510 animals versus WTs (Figure 2I). We also examined neuronal responses in CA1 neurons to ripple events and found that burst spike rates were significantly suppressed in APP/PS1-rTg4510 animals relative to WTs and that this suppression effect was greater than that observed in single-spike firing responses to these events (Figures 2J, 2K, and S1D–S1F). Thus, these results indicate an AD pathology-dependent breakdown in the prevalence and burst-mediated magnitude of circuit-level processes known to support learning and memory.

Impaired bursting in CA1 neurons is tau dependent and concurrent with debilitated theta-phase coding

The observed deficit in bursting could be underpinned by the effects of either Aβ or tau pathology or the presence of both.

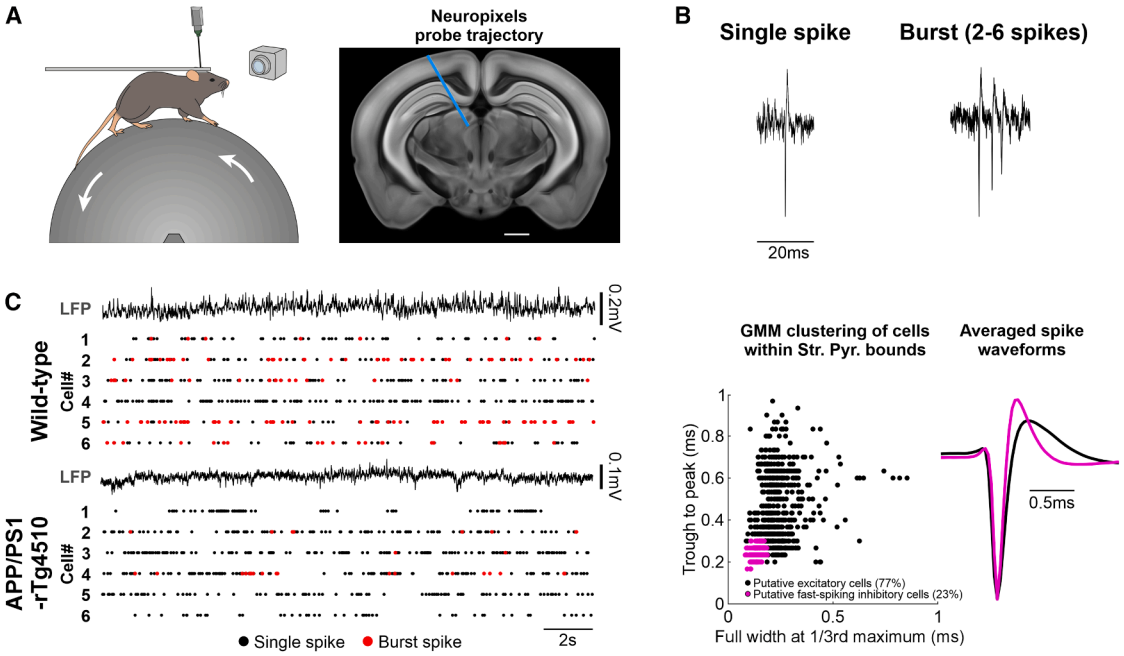

Figure 1. Examination of neuronal burst firing in hippocampus CA1 of the head-fixed awake mouse indicating suppressed bursting in APP/PS1-rTg4510 mouse model expressing both Aβ and tau pathology

(A) Top left, schematic illustrating Neuropixels recording setup in awake head-fixed mice, with right showing probe trajectory overlaid on Allen Common Coordinate Framework (CCF) atlas image and implantation into left hippocampus CA1 (scale bar, 1 mm).

(B) Normalized examples of a single spike and a burst event (defined as 2–6 spikes with ISIs <10 ms).

(C) Left, example 20-s recording of LFP activity in CA1 and concurrent neuronal spiking activity raster of six putative excitatory CA1 neurons, with black markers indicating single spikes and red markers indicating burst-related spikes, in a WT mouse and APP/PS1-rTg4510 mouse with both human Aβ and tau. Right, outcomes of clustering spike waveform parameters from units within putative CA1 pyramidal layer (Str. Pyr., see Figure S1A), using Gaussian-mixture modeling (GMM). Far right, averaged spike waveforms for each cluster, with cluster 2 (magenta) being associated with the fastest waveform dynamics and classified as putative fast-spiking inhibitory interneurons and cluster 1 (black) being classified as (primarily) putative excitatory neurons (colors as in left panel).

See also Figure S1.

Consequently, we next sought to dissect the principal proteinopathic driver of impaired bursting. Recapitulating our *in vivo* Neuropixels recording approach under conditions of light isoflurane anesthesia (~1%), which can promote neuronal bursting,[27,28] we first examined the ISI distribution of putative excitatory CA1 neurons in 7- to 9-month-old APP/PS1 (Aβ pathology only), rTg4510 (tau pathology only), and APP/PS1-rTg4510 mice, versus WT controls. Similarly to our awake data, we again observed a dramatic loss of the 2–6 ms intra-burst ISI peak in neurons from APP/PS1-rTg4510 mice versus those from WTs (Figure 3A). Remarkably, rTg4510 mouse neurons closely mirrored this impairment with a similar temporal structure of neuronal firing, while APP/PS1 mouse neurons, in contrast, exhibited an amplified intra-burst ISI peak (Figure 3A). These changes were also reflected by a reduction in the burst index (proportion of ISIs < 10 ms) of neurons from both rTg4510 and APP/PS1-rTg4510 mice relative to those from WTs and an increase in those from APP/PS1 animals (Figure 3B). While there was considerable variability in "burstiness" (i.e., burst index) across neurons, as previously reported,[5,13] albeit notably less so in neurons from tau-bearing mice, the overall pattern of genotype-specific differences was preserved across a range of intra-burst ISI thresholds from 4 to 12 ms (Figure S1G). Importantly, the observed tau-associated reduction in neuronal bursting behavior appeared not to be a rTg4510-specific phenotype, since neurons from an alternative tau-bearing PS19 mouse model[29] at 9 months of age also exhibited impaired bursting behaviors (Figures S1H–S1K). Further, the probability of observing single spikes, or two or more spikes within a burst event, decreased roughly exponentially in neurons from WT mice (as previously reported and reflected by a near-linear fit on a logarithmic scale[5,22]), with similar characteristics in APP/PS1 neurons (Figure 3C). In contrast, the probability of observing single spikes and burst-related spikes in both rTg4510 and APP/PS1-rTg4510 neurons decreased comparatively more steeply and was associated with a remodeling of spike output mode toward an increased probability of single spikes and reduced probability of burst spikes relative to controls (Figure 3C). Taken together, these data provide evidence for a tau-dependent reduction in not only the incidence but also the complexity of neuronal bursting events. This could have important implications for the ability of neurons to transmit information to downstream targets[30] and to participate in oscillatory-related network-level processes that support memory-based cognition.

To investigate whether impaired bursting indeed occurred alongside a disrupted synchronization of neuronal spiking

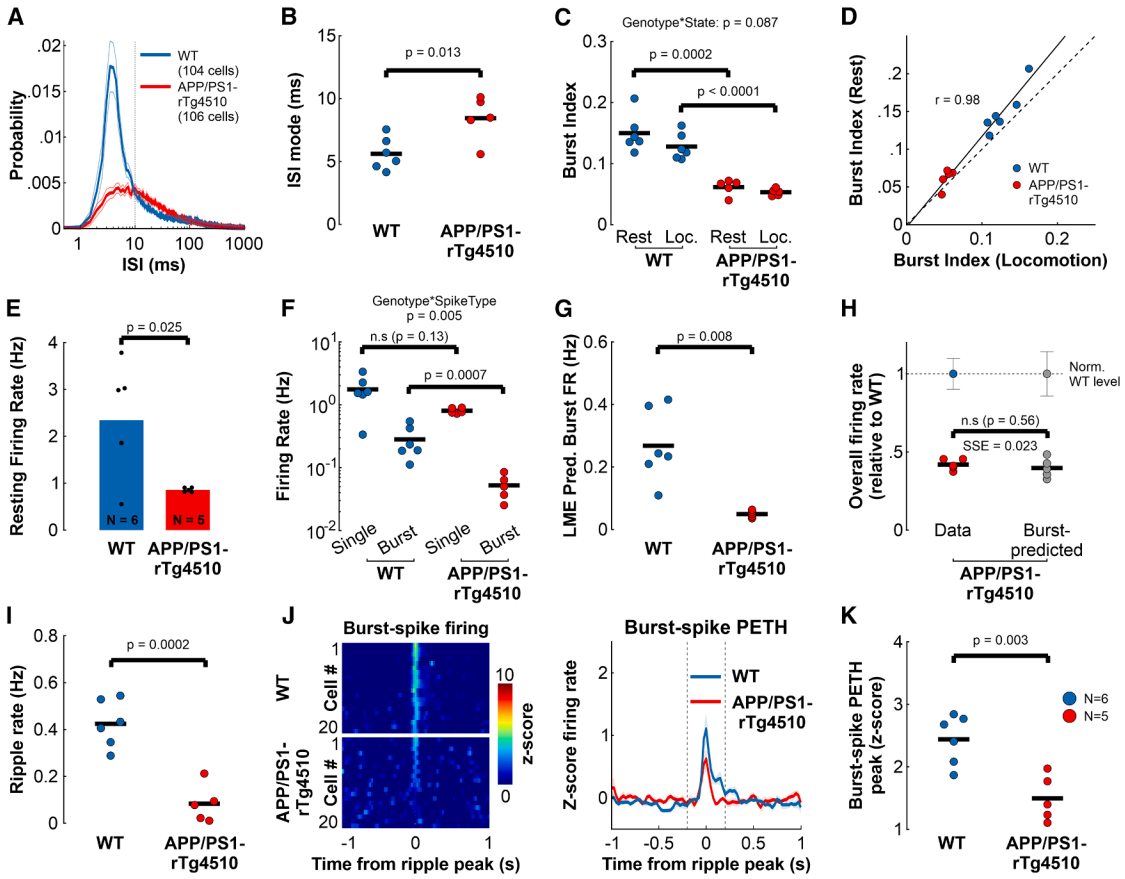

Figure 2. AD pathology suppresses neuronal bursting in hippocampus CA1 of awake mice

(A) ISI histogram averaged across WT and APP/PS1-rTg4510 neurons and revealing a loss of intra-burst ISI peak (~2–6 ms) across behavioral states in APP/PS1-rTg4510 animals. Error bars are SEM, and means from n = 104 WT and 106 APP/PS1-rTg4510 neurons from a single experimental session across animals. Dashed gray line at 10 ms.

(B) This effect was paralleled by a significant increase in the ISI mode at the animal level (most frequently observed ISI; data represent, for each animal, the median ISI mode across neurons within each session, averaged over sessions (20.2 ± 2.3 neurons/animal/session), in APP/PS1-rTg4510 mice (N = 5) relative to WT (N = 6). Unpaired t test, T(9) = −3.07, p = 0.013. Black bars indicate means, with each datapoint representing an individual animal.

(C) Reduced propensity for neuronal bursting during resting and locomotion behaviors in APP/PS1-rTg4510 mice (N = 5) relative to WT (N = 6). Two-way mixed ANOVA suggesting significant interaction between genotype and behavioral state, F(1,9) = 3.69, p = 0.087, with Tukey-Kramer posthoc comparisons. Black bars indicate means, with each datapoint representing an individual animal.

(D) Neuronal bursting was stable across resting and locomotion behaviors, with no significant difference in slopes between genotypes, ANCOVA F(1,7) = 0.11, p = 0.75. Solid line denotes least-squares linear fit across genotypes, with Pearson's correlation coefficient given as inset. Each datapoint represents an individual animal (N = 6 WT, N = 5 APP/PS1-rTg4510), with dashed line showing reference line with unity slope.

(E) APP/PS1-rTg4510 mice (N = 5) exhibited a significant reduction in neuronal firing rates relative to WT (N = 6). Welch's t test, T(5.02) = 3.16, p = 0.025, bars indicating means with error bars as SEM, with each datapoint representing an individual animal.

(F) Burst spike firing, but not single-spike firing, is significantly reduced during the resting state in APP/PS1-rTg4510 mice (N = 5) relative to WT (N = 6). Two-way mixed ANOVA following log transformation indicating significant interaction between genotype and spike type, F(1,9) = 13.8, p = 0.005, with Tukey-Kramer post hoc comparisons. Black bars indicate means, with each datapoint representing an individual animal.

(G) Burst firing rates remained significantly reduced in APP/PS1-rTg4510 mice versus WTs after accounting for baseline firing rates, genotype differences, and subject-specific variability using a linear mixed-effects (LME) model (performed on log transformed data as above; fixed effects coefficients: intercept, −1.86 [−2.4–1.3, 95% CI], tStat = −8.1, p < 0.0001; baseline firing rate, 0.65 [0.08−1.2, 95% CI], tStat = 2.6, p = 0.03; genotype [APP/PS1-rTg4510], −1.1 [−1.8–0.36, 95% CI], tStat = −3.48, p = 0.008; dF = 8 in all cases). Black bars indicate means, with datapoints representing the exponentiated fitted responses from the LME model for each individual animal.

(H) Simple linear modeling of the relationship between burst firing rates and overall firing rates (i.e., the sum of single and burst spiking; see Figure S1B) was sufficient to accurately predict the experimentally observed debilitation in overall firing rates in APP/PS1-rTg4510 mice (~60% reduction) relative to WTs. No significant difference was observed between empirical and modeled data, paired t test, T(4) = 0.64, p = 0.56, with sum of squares due to error (SSE) given as inset. Black bars indicate means, with each datapoint being paired and representing an individual animal (N = 5 APP/PS1-rTg4510). Dashed line at y = 1 denotes the normalized overall firing rate across WTs for comparison, with error bars denoting 95% CIs.

(I) The incidence of high-frequency ripples was significantly reduced in APP/PS1-rTg4510 mice (N = 5) versus WTs (N = 6). Unpaired t test, T(9) = 6.12, p = 0.0002, black bars indicate means with each datapoint representing an individual animal.

(legend continued on next page)

outputs with ongoing network oscillations, we examined the degree of temporal coordination between neuronal spike timing and local theta frequency oscillations in the hippocampal local field potential (LFP). Calculation of the spike-LFP phase-locking value (PLV) for individual CA1 neurons revealed a prominent peak in WT neurons in the theta frequency range (~4–8 Hz), which was absent as well as inverted in rTg4510 neurons (Figure 3D). Moreover, we also found a significant positive correlation between theta-PLV peak amplitude and burst index across animals (Figure S1L). An associated phase code in hippocampus pertains to theta-phase modulation of faster gamma-frequency LFP oscillations (30–100 Hz). On this basis, we quantified the cross-frequency coupling between theta phase and gamma amplitude and observed that not only was this metric significantly reduced in rTg4510 mice relative to WTs (Figures 3E and 3F), but that it also correlated to burst index across animals (Figure S1M). Notably, reduced theta-gamma coupling has been reported in humans with early symptomatic AD,[31] but the underlying neuronal determinants have remained unknown. These results, in combination with our earlier findings (Figure 2), suggest that tau pathology selectively attenuates the intrinsic bursting of CA1 hippocampal neurons, consequently inducing a shift in spike output mode toward single-spike firing, desynchronizing neuronal firing with ongoing network oscillatory activity and impairing the hippocampal theta-phase code of relevance to cognition.[32–34]

Impaired bursting emerges before abundant tau tangle pathology and is associated with reduced neuronal expression of CaV2.3 R-type calcium channels

We next posited that the observed tau-related impairment in bursting would already be detectable prior to substantial neurofibrillary tau tangles, since soluble tau species have been suggested to be detrimental to neuronal function *in vivo*.[3,4] We therefore conducted *in vivo* whole-cell patch-clamp recordings in rTg4510 mice of 2–3 months of age, which have elevated levels of soluble tau without prominent tangle pathology in the hippocampus,[3] and compared spontaneous bursting characteristics of hippocampal CA1 pyramidal neurons with those of littermate controls (Figure 4A). Consistent with our hypothesis and previous results (Figures 2 and 3), we again found reduced bursting in rTg4510 mice (~80% of neurons failing to generate spontaneous bursts), compared with WTs (Figure 4B), as well as a relative reduction in the number of spikes within burst events in the tau-bearing animals (Figure 4C).

CA1 burst firing *in vivo* has been previously shown to critically depend on both NMDA receptors and CaV2.3 (R-type) voltage-gated calcium channels.[28,35–37] We thus performed immunohistochemical analysis of the obligatory NMDA-receptor subunit NR1 and CaV2.3 in CA1 of 2- to 3-month-old rTg4510 mice and WT littermate controls. Notably, we found that neuronal expression of CaV2.3 was significantly reduced in rTg4510 mice, compared with controls (Figures 4D and 4E), while NR1 was not prominently different between genotypes at this young age (Figures S2A and S2B).

In order to confirm that these impairments were tau dependent, we leveraged the doxycycline (Dox)-repressible human tau transgene present in rTg4510 mice to suppress *de novo* production of soluble tau.[3,4] To this end, 3-month-old rTg4510 mice were fed Dox in chow for 3 months and compared with rTg4510 mice on a standard diet at 6 months of age, following previous protocols.[3,4,38] Immunohistochemical analysis revealed a significant increase in somatic CaV2.3 expression in CA1 of Dox-treated animals versus untreated controls, suggesting that an impairment of CaV2.3 expression was indeed tau dependent (Figures 4F and S2C). We subsequently examined how tau transgene suppression by Dox treatment impacted on different tau species within the same animals. In particular, we were interested in a rare HMW species of soluble hyperphosphorylated tau found to be present not only in AD patients but also, importantly, in the rTg4510 and PS19 mouse models used in our study.[39,40] Notably, HMW tau can potently seed anatomically connected regions and propagate across neural systems, is closely linked to the rate of clinical progression in AD patients, and can be extracted by size-exclusion chromatography (SEC).[1,40–42] In turn, low molecular weight (LMW) monomeric and dimeric tau represents the vast majority of soluble tau in the AD brain, predominates in healthy control brain, and has previously been shown to have limited seeding capacity relative to HMW tau.[1,40] Western blot experiments revealed a significant reduction of total tau levels by Dox treatment, in line with previous studies[3,4,38] (Figure S2D). Notably, we found a significantly greater suppression of HMW tau, relative to LMW tau, in Dox-treated animals versus untreated controls (Figures 4G and S2D–S2F), suggesting a preferential effect of the treatment on HMW tau species.

Next, we asked whether an increase in somatic CaV2.3 expression and a reduction in tau levels were associated with an amelioration of impaired neuronal burst dynamics. Thus, we performed awake Neuropixels recordings (as previously) in the same rTg4510 mice that had undergone Dox treatment prior to sacrifice and exploited an inherent variability in treatment efficacy to examine the impact of varying levels of HMW and LMW tau on neuronal bursting in CA1. This analysis, incorporating linear mixed-effects modeling, indicated that lower levels of HMW tau, but not LMW, were associated with a progressive increase in the probability of observing faster and more complex burst events (i.e., those with shorter ISIs and a greater number of constituent spikes) (Figures 4H–4J; Table S1).

(J) Peri-event time histograms (PETHs) of neuronal bursting responses to ripple events. Left, heat maps illustrate *Z* scored burst firing rates of top 20 responding hippocampal neurons for each genotype. Right, averaged burst firing PETHs with solid lines as means across animals for each genotype ($N = 6$ WT, $N = 5$ APP/PS1-rTg4510), and error bars as SEM.

(K) Quantification of peak firing rate responses to ripple events (maximum *Z* score within ±0.2 s of ripple peak, see dashed lines in (J), showing a significant reduction in burst spike firing in APP/PS1-rTg4510 mice ($N = 5$) versus WTs ($N = 6$). Unpaired t test, $T(9) = 4.1$, $p = 0.003$, black bars indicate means with datapoints representing the average across neurons for each individual animal.

See also Figure S1.

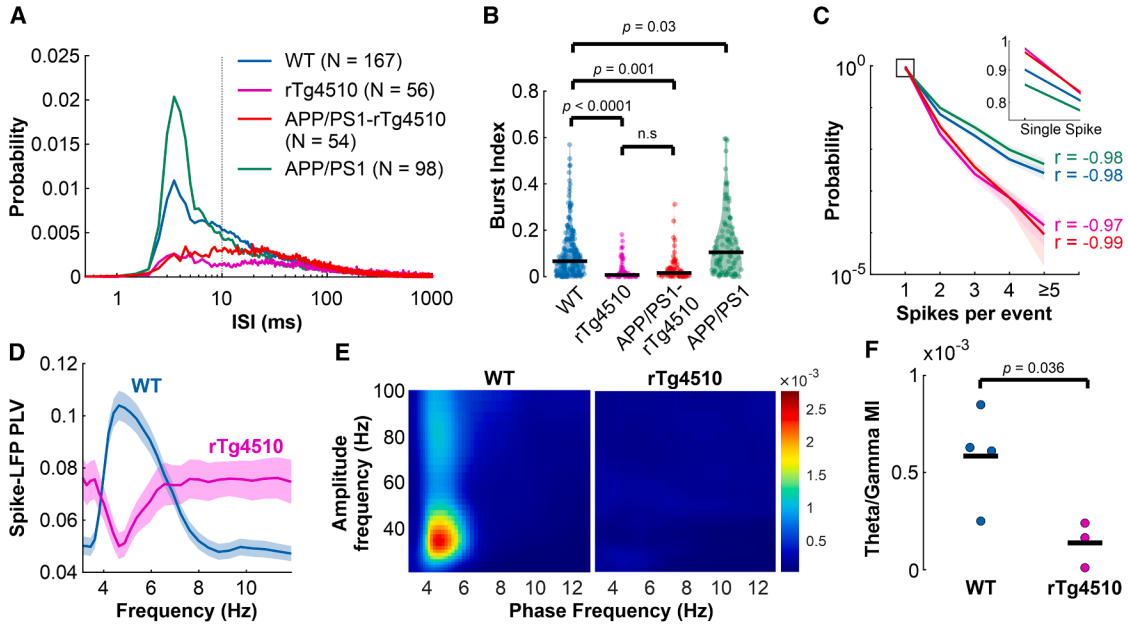

Figure 3. Tau pathology specifically suppresses neuronal bursting and allied theta-phase coding in hippocampus CA1 *in vivo*

(A) Averaged ISI histogram of WT, rTg4510, APP/PS1-rTg4510, and APP/PS1 neurons during light isoflurane anesthesia, revealing loss of intra-burst ISI peak in rTg4510 and APP/PS1-rTg4510 neurons versus WT. Error bars omitted for clarity, with cell numbers for each genotype given in inset. Dashed gray line at 10 ms.

(B) Quantification showing a significant reduction in burst index of rTg4510 and APP/PS1-rTg4510 neurons versus those from WTs. LME model with WT as reference level; fixed effects coefficients: intercept, 0.10 [0.09 0.12, 95% CI], tStat = 12.15, $p < 0.0001$; APP/PS1, 0.04 [0.011 0.067, 95% CI], tStat = 2.79, $p = 0.005$; rTg4510, −0.076 [−0.11–0.04, 95% CI], tStat = −4.44, $p < 0.0001$; APP/PS1-rTg4510, −0.065 [−0.1–0.03, 95% CI], tStat = −3.77, $p = 0.0002$ (dF = 371 in all cases). Post hoc pairwise comparisons with Bonferroni correction for multiple comparisons. Black bars indicate medians with each datapoint denoting a single neuron; cell numbers given in (A) across 4 (WT) or 3 mice per genotype.

(C) The probability of observing single spikes and *n* spikes during a burst event decreased approximately exponentially and similarly in neurons from WT and APP/PS1 mice but more steeply in rTg4510 and APP/PS1-rTg4510 neurons and with a corresponding increase in probability of observing single spikes (inset). Error bars are SEM, cell numbers given in (A) across four (WT) or three mice per genotype. Pearson correlation coefficients (r) for each genotype given in inset.

(D) Spike-LFP PLV at theta frequencies (4–8 Hz) was impaired in rTg4510 neurons versus WT neurons (note inverted peak at ∼5 Hz). Error bars are SEM; $N = 167$ WT, 56 rTg4510 neurons across 4 (WT) or 3 (rTg4510) mice.

(E) Comodulograms showing cross-frequency modulation index (MI) in CA1 as a function of phase frequency and amplitude frequency and averaged across animals for each genotype ($N = 4$ WT, 3 rTg4510 mice). Hot colors indicate larger modulation.

(F) Quantification indicating that the averaged MI between theta frequencies and gamma oscillations (30–100 Hz) was significantly reduced in rTg4510 animals versus WTs. Unpaired t test, T(5) = 2.84, $p = 0.036$, black bars indicate means with each datapoint denoting a single animal ($N = 4$ WT, 3 rTg4510 mice).

See also Figure S1.

Taken together, these results strongly implicate soluble forms of tau, and HMW species in particular, as key mediators of impaired bursting in hippocampus CA1 and identify a selective downregulation of CaV2.3 as a putative underlying mechanism, consistent with previous results showing that CaV2.3 antagonists alone are sufficient to block CA1 neuronal bursting.[35,36]

AD patient-derived HMW forms of soluble oligomeric tau selectively suppress bursting in hippocampal neurons

To establish the relevance of our findings to human disease and to determine whether HMW tau derived from the human AD brain could similarly impair bursting of hippocampal neurons, we isolated HMW tau in postmortem brain extracts from an AD patient using established protocols[1,40,42] (Figure S3A) and conducted hippocampal slice whole-cell patch-clamp recordings in CA1 pyramidal neurons of WT mice (Figure 5A). Notably, the tau derived from this particular patient (84-year-old male, Braak stage VI, Thal stage V) has been previously extensively characterized (see patient AD7 in Kumar et al.[41]). The patch micropipette was pre-loaded with an internal solution supplemented by varying concentrations (0.1–10 nM) of the patient-derived HMW tau SEC fraction to allow diffusion of tau into the neuronal somata, thus reproducing the early pathological redistribution of tau into the somatodendritic compartment that precedes tangle formation.[43] To examine the subsequent effects on neuronal function, we established a paradigm for long-term (>60 min) recordings involving multiple sequential current step injections (−50 to 400 pA), repeated seven times at intervals of 10 min[44] (Figure S4A). These experiments revealed that somatic infusion of HMW tau at 10 nM induced a marked reduction in neuronal bursting events, but not single spikes, consistent with our *in vivo* data. This effect was especially prominent at the maximum 400-pA current step, at which ∼90% of neurons failed to generate a burst event, and was notably absent at lower HMW concentrations (Figures 5B–5D and S4B–S4E). While the exact amount of HMW tau that is present intracellularly in the human

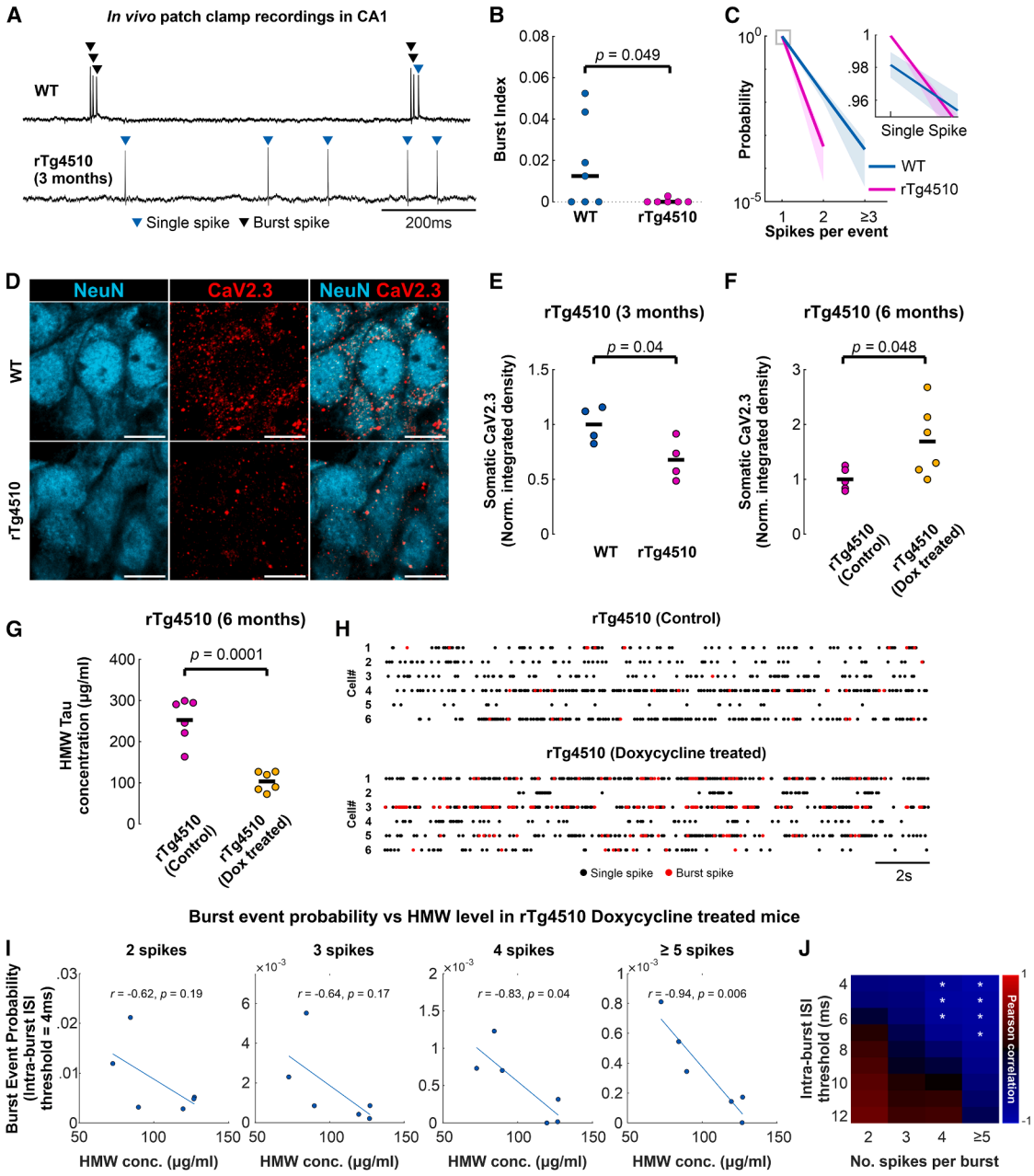

Figure 4. Bursting impairments in CA1 neurons are independent of substantial tangle pathology and are linked to reduced somatic CaV2.3 expression and elevated levels of soluble HMW tau

(A) Example *in vivo* whole-cell patch-clamp recordings of spontaneous activity in CA1 pyramidal neurons from a young (3 months old) WT and rTg4510 mouse, with single and burst spikes indicated (blue and black triangles, respectively).

(B) The propensity for bursting (bursting index) in young rTg4510 mouse neurons was significantly reduced relative to WTs (one-tailed Wilcoxon rank-sum test [rank-sum statistic = 59.5], $p < 0.05$, black bars indicate medians, each marker denotes an individual animal, $N = 7$ WT, 6 rTg4510).

(C) The probability of observing two or more spikes within a burst decreased more steeply in rTg4510 mouse neurons versus WTs, with the probability of observing single spikes correspondingly increased.

(D) Example immunofluorescent images showing NeuN (cyan) and CaV2.3 (red) in the pyramidal layer of CA1 of 3-month-old WT (top) and rTg4510 (bottom) mice. Scale bars represent 10 µm.

(E) Quantification of the integrated density of somatic CaV2.3 staining, normalized to soma area and WT condition, indicating a significant reduction in somatic CaV2.3 in CA1 of rTg4510 mice relative to WTs (unpaired t test: $T(6) = 2.578$, $p = 0.04$). Each marker represents an individual animal ($N = 4$ for each genotype), with black bars denoting means.

(legend continued on next page)

brain is not known with certainty, we have previously measured that the tau concentration in human neurons is of the order of 1–10 μM[45] and have estimated that HMW tau represents ~1% of total tau levels in the human cortex.[40] These data thus suggest that 10 nM HMW tau is positioned well within an appropriate range to reproduce the (patho)physiological effects of HMW tau in human AD neurons.

To investigate these findings further, we repeated the experiments using LMW monomeric and dimeric tau derived from the same AD patient brain extract (Figure S3A). As additional independent controls, we used 10 nM concentration LMW and HMW fractions that importantly had both been immunodepleted for tau using HT7 antibody (Figure S3B). These experiments demonstrated that neither 10 nM LMW tau nor immunodepleted fractions recapitulated the electrophysiological suppressive effect of 10 nM HMW tau on neuronal bursting (Figures 5E–5H and S5). Following the same protocols, we repeated these experiments using LMW tau derived from the brain of a control subject (89-year-old female at Braak stage I and Thal stage 0; examination of HMW was not possible due to the very low concentration of this species in the control brain; Figures S3A and S3B[46]). Similarly, these experiments showed no effect of 10 nM LMW tau on neuronal bursting versus immunodepleted tau fraction, further refuting a role for human LMW tau as a driver of bursting impairments (Figure S6). Indeed, the effect of 10 nM HMW tau persisted when compared with additional control conditions where either no additional solutes or PBS alone was added to the patch pipette solution (Figures S7A and S7B). Furthermore, to independently assess whether recombinant tau, lacking the more complex biochemical states characteristic of tau extracted from the human AD brain, could also impair bursting, we compared recombinant *E. coli*-derived (monomeric, unphosphorylated) or SF9-derived (oligomeric, hyperphosphorylated) forms of tau[45] versus GAPDH (as a control to ensure any effect from recombinant proteins was not attributable to intracellular introduction of non-native proteins). Notably, these recombinant species did not recapitulate bursting deficits even when administered at relatively high micromolar concentrations (Figures S7C and S7D). Taken together, these findings suggest that soluble HMW tau species specifically cause a bursting impairment of CA1 hippocampal neurons.

DISCUSSION

We present evidence for a pathophysiological impact of human tau at the single-neuron level, namely, the suppression of complex spike burst firing in hippocampus CA1, which represents a key cellular mechanism underpinning memory-guided cognition. We further demonstrate that impaired bursting compromises circuit-level mechanisms that are fundamentally intertwined with this burst spike output mode. Mechanistically, these functional impairments occurred alongside a marked downregulation of CaV2.3 channels that was ameliorated by tau suppression and which are critical for burst firing *in vivo*. We conclude by identifying soluble HMW tau, in mouse models and that isolated from the AD patient brain, as the tau species specifically responsible for potently diminishing the ability of hippocampal neurons to generate burst firing.

Our data thus provide a cellular explanation for recent findings whereby the amount of HMW tau correlates closely with the rate of AD clinical progression[1,40–42] and, more broadly, suggests a neurophysiological mechanism (i.e., impaired bursting) linking tau accumulation and clinical symptoms in AD. Indeed, CA1 neuronal bursts are associated with dendritic plateau potentials and promote the rapid generation of spatial (e.g., place cells) and non-spatial representations in the hippocampus through BTSP.[16,47,48] In addition, bursts in CA1 neurons are linked to c-Fos expression and contribute to the formation and reactivation of memory engrams.[49,50] Furthermore, bursts are transmitted as gain-modulated firing rate increases to downstream targets,[30] where a reduced ability to generate bursts could contribute to a tau-dependent functional disconnection of the hippocampus and other brain regions, as reported in humans.[51] Notably, neurons with a high intrinsic bursting propensity may be particularly suited to support memory-related processes by acting as critical determinants of hippocampal population codes and being preferentially recruited during memory encoding and adaptive plasticity.[5,13,16,17] Our observations that, in the presence of tau pathology, neuronal populations not only burst less but also

(F) Quantification of the integrated density of somatic CaV2.3 staining in 6-month-old untreated control and Dox-treated rTg4510 mice, normalized to soma area and control condition, indicating a significant increase in somatic CaV2.3 in CA1 of Dox-treated rTg4510 mice relative to controls (Welch's unpaired t test, T (6.15) = −2.5, p = 0.048). Each marker represents an individual animal (N = 5 untreated, N = 6 treated), with black bars denoting means.

(G) HMW tau concentration in untreated control and Dox-treated rTg4510 mice brains (same animals as in F), indicating a significant suppression of HMW tau by Dox treatment (unpaired t test, T(10) = 6.2, p = 0.0001). Each marker represents an individual animal (N = 6 untreated, N = 6 treated), with black bars denoting means.

(H) Example 20-s neuronal spiking activity raster of six putative excitatory CA1 neurons, with black markers indicating single spikes and red markers indicating burst-related spikes, in an untreated awake rTg4510 control mouse (top) and a Dox-treated awake rTg4510 mouse (bottom). Note the increase in number of burst spikes in the Dox-treated (tau-suppressed) rTg4510 mouse.

(I) Relationship between HMW concentration and the probability of observing a burst event with 2, 3, 4, or ≥5 spikes, at an intra-burst ISI threshold of 4 ms, in Dox-treated awake rTg4510 mice. Note the progressively increasing inverse correlation with increased burst complexity (left to right). Each datapoint represents an individual animal (N = 6) with linear fit as blue line, and Pearson correlation coefficient (r) and associated p value provided as inset in each panel.

(J) Correlation matrix showing the Pearson correlation coefficient for the relationship between HMW concentration and the probability of observing a burst event in Dox-treated rTg4510 mice (values at y = 4 ms are the same as in I) across all examined intra-burst ISI thresholds (4–12 ms, y axis) and burst complexity values (number of spikes per burst, 2–≥5, x axis). Cold colors indicate a negative correlation. Data from N = 6 mice for each comparison. Note the progressively stronger negative correlation for faster and more complex burst events, where asterisks indicate correlation $p < 0.05$ (uncorrected for multiple comparisons). See Table S1 for LME modeling, indicating a significant effect of HMW tau, but not LMW, on burst event probability.

See also Figure S2.

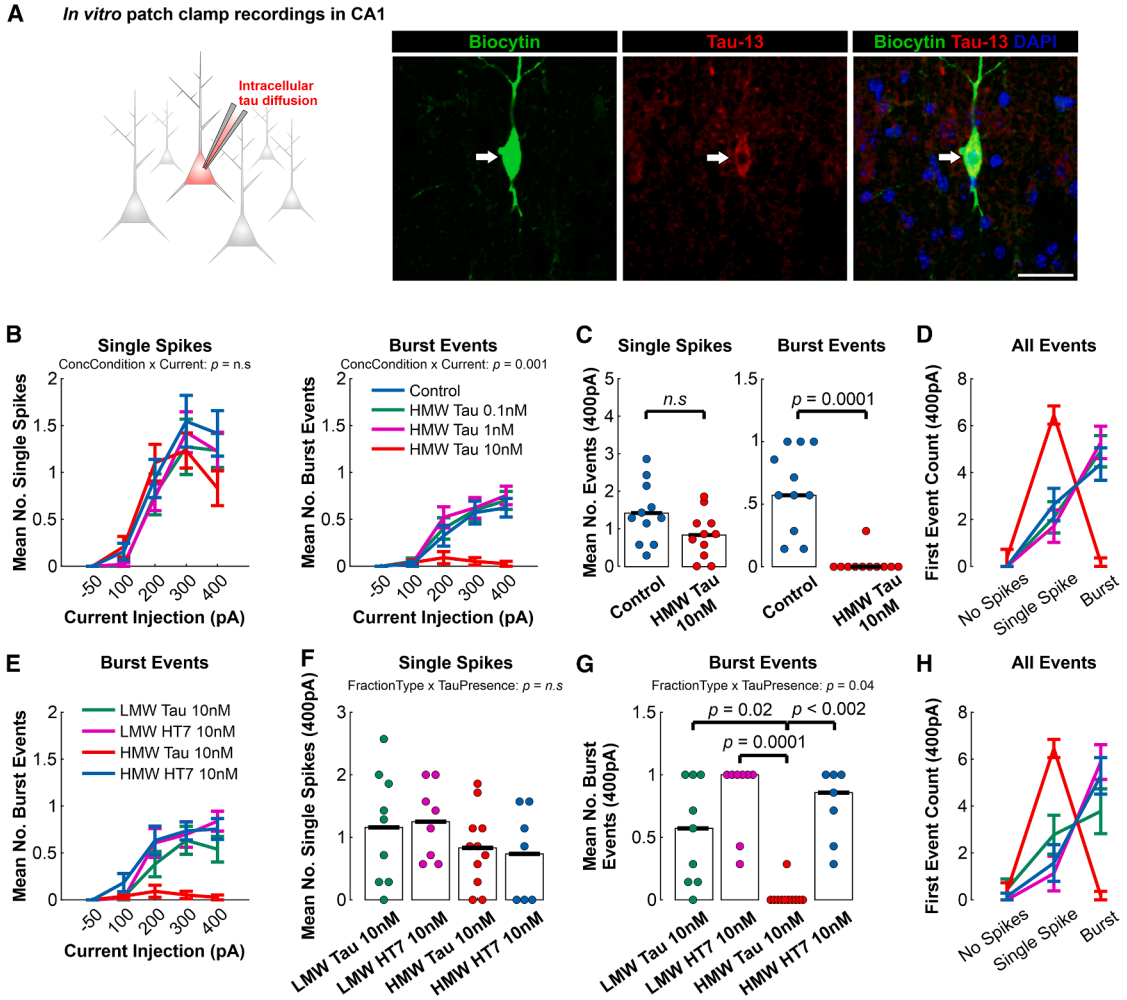

Figure 5. AD patient-derived HMW tau species impair burst spiking in CA1 hippocampal neurons

(A) Left, schematic of hippocampal slice patch-clamp recordings in CA1 pyramidal neurons in which tau was added to micropipette prior to breakthrough and allowed to diffuse intracellularly. Right, immunofluorescence images showing biocytin (green) and Tau-13 (red) in a CA1 pyramidal neuron (DAPI nuclear stain shown in blue), following *in vitro* hippocampal slice patch-clamp recordings, and exemplifying diffusion of soluble tau (hyperphosphorylated recombinant SF9 derived) from patch pipette into somatodendritic compartments. Scale bar represents 25 μm.

(B) Left, no significant interaction between current step (−50 to 400 pA) and HMW tau condition (control, 0.1–10 nM) on incidence of single spikes. Two-way mixed ANOVA, CurrentStep × concentration condition, $F(12,172) = 0.96$, $p = 0.42$ with lower bound adjustment. Right, significant interaction between current step and HMW tau concentration condition on incidence of burst events. Two-way mixed ANOVA, CurrentStep × concentration condition, $F(12,172) = 6.62$, $p = 0.001$ with lower bound adjustment. Note markedly reduced incidence of bursts in 10-nM HMW tau condition. Data denotes average over series/time during first 50 ms of current step, with error bars as SEM, from $N = 11$ (control), 11 (0.1 nM), 14 (1 nM), and 11 (10 nM) cells. The control condition pertains to HT7 immunodepleted fraction prepared using the same volume as for the 0.1-nM HMW tau condition solution.

(C) Quantification of effect of 10 nM HMW tau at the maximum depolarizing current injection step of 400 pA, indicating no effect on incidence of single spikes (left, black bars indicate means, unpaired t test $T(20) = -1.9$, $p = 0.07$) but a significant suppression of bursting (right, black bars indicate medians, Wilcoxon rank-sum test [rank-sum statistic = 184.5], $p = 0.0001$) versus control. $N = 11$ cells in all conditions.

(D) Examination of the first spiking event following 400-pA depolarizing current injection step, indicating increased propensity for single spikes, rather than burst events (two or more spikes), in the presence of 10 nM HMW tau, in contrast to lower HMW concentrations and control.

(E) Comparison of effects of LMW and HMW 10 nM tau from the same patient brain extract and associated fractions immunodepleted for tau with HT7 antibody, as a function of current injection, indicating a pronounced suppressing effect by 10 nM HMW tau on bursting. Data denote average over series/time during first 50 ms of current step, with error bars as SEM. $N = 9$ (LMW tau 10 nM), 8 (LMW HT7), 11 (HMW tau 10 nM), and 7 (HMW HT7) cells.

(F) Quantification of effects at 400-pA current injection step, indicating no species- or tau-specific effect on single spikes (two-way ANOVA, FractionType × TauPresence $F(1,31) = 0.15$, $p = 0.7$, black bars indicate means).

(legend continued on next page)

exhibit reduced variability in burst propensity, suggest that tau may not only impair the overall capacity of a system to generate bursts, but it also constrains the dynamic range of neuronal firing patterns. A reduced capacity to engage a neuronal population with the sufficient heterogeneity and breadth of burst firing patterns to flexibly meet demands may thus potentially limit the ability of the hippocampus to adaptively encode and integrate new information.[13] Together, these observations suggest that impaired CA1 neuronal bursting could provide a unifying explanation for the tau-related impairment of network connectivity and subsequent decline in memory-based cognition observed in AD.

We also observed that the firing rates of single spikes were relatively preserved and that there was a small increase in the probability of this spike output mode relative to burst events, suggesting that tau-bearing neurons may potentially compensate for an impaired burst output by adaptively modulating single-spike firing. However, bursts represent a distinct firing mode that is considered crucial for hippocampal information processing, synaptic plasticity, and memory formation. Moreover, homeostatic plasticity mechanisms are increasingly recognized to be impaired in AD.[52] Thus, compensatory mechanisms that counteract a loss of bursting may progressively deteriorate as tau pathology becomes more abundant and attendant with age-related reductions in bursting,[53] ultimately reducing the capacity of the hippocampus to sustain normal information processing and network function.[54]

The misfolded and aggregated tau underlying these impairments is thought to arise through age-related changes in proteostasis and impaired clearance mechanisms that become more pronounced over time. These early tau aggregates are thought to then seed and promote further tau misfolding and oligomerization, giving rise to HMW tau forms that become increasingly resistant to degradation. Indeed, prior work has shown that HMW tau can potentiate further tau aggregation and spreads across anatomically connected brain regions,[42] a pathological process that may well be accelerated by age-related decline in proteasomal and autophagic function.[45] As a result, misfolded tau appears to impact normal electrophysiological bursting activity patterns of hippocampal excitatory neurons, both *in vivo* and in slice preparations, using mouse models and extracts from the human AD brain. In turn, once disrupted, these processes may further accelerate the disease course by promoting circuit-level dysfunction, including decreased ripple rate, weakened theta-gamma coupling, and abnormal neural synchrony. We consider the possibility that similar effects occur in human AD, where neural system disruption would then be viewed as consequent to both neuronal loss and dysfunction of remaining, structurally intact, neurons that are impacted by tau. We speculate that the latter could contribute to the emergence of cognitive symptoms in AD patients and, in principle, may potentially provide an important therapeutic target, since reduction of tau (at least in the mouse) is found to improve function. Notably, our results indicate that for any such treatments to be effective, they need to be capable of reducing intracellular HMW tau, which represents a mere ~1% of all soluble tau in the AD brain and is present in the nanomolar range within AD neurons.[45] In addition to targeting these rare tau species, we propose that the restoration of neuronal bursting, potentially through modulation of CaV2.3 channels, represents a novel and complementary target for therapeutic intervention in AD.

Limitations of the study

In interpreting our results, it is also important to consider limitations to the study. Our *in vitro* patch-clamp datasets concerning human-derived HMW tau were performed using extracts from a single human (male) AD brain. However, we have examined within-patient batch effects and observed stable tau bioactivity, with multiple preparations from the same patient sample yielding analogous outcomes across our previous studies.[42,55] Future studies could extend beyond AD and examine whether non-AD HMW tau, or indeed other tau species, in differing tauopathies produce similar effects on bursting. Notably, our *in vivo* findings in tau-bearing mice indicated that the neuronal bursting deficit is contingent on HMW concentration in the brain, suggesting that variability in the levels of this protein across human samples might modulate the magnitude, rather than the presence, of this effect. Furthermore, our experiments identified reduced expression of CaV2.3 channels (but not of NR1) as a potential mechanism underlying HMW-driven bursting deficits in CA1 neurons, although the precise mechanistic pathways by which HMW tau might modulate CaV2.3 expression were not investigated and thus merit further examination in future studies. We also acknowledge that our findings do not exclude the possibility of additional contributions by other processes (e.g., loss or gain of function in other channel types or alterations in dendritic excitability) not investigated in the current study. Further, while we did not formally test for sex differences in our mouse-derived data, we employed mixed-sex cohorts to mitigate potential sex-related biases and strengthen the robustness and generalizability of our findings.

RESOURCE AVAILABILITY

Lead contact

Further information and requests for resources and reagents should be directed to and will be fulfilled by the lead contact, Marc Aurel Busche (m.busche@ucl.ac.uk).

Materials availability

This study did not generate new unique reagents.

Data and code availability

- Source data for quantitative comparisons presented herein will be deposited at Zenodo (https://doi.org/10.5281/zenodo.15044305) and made publicly available as of the date of publication.

(G) Evidence for a species- and tau-specific effect of 10 nM HMW tau at 400 pA on incidence of bursting events (two-way exploratory ANOVA for estimation of interaction, FractionType × TauPresence $F(1,31) = 4.75$, $p = 0.04$, followed by Kruskal-Wallis test, chi-sq(3) = 22.5, $p = 0.0001$ and Tukey-Kramer post hoc comparisons, black bars indicate medians).

(H) Examination of the first spiking event following 400-pA depolarizing current injection step, again indicating increased propensity for single spikes, rather than burst events (two or more spikes), in the presence of 10 nM HMW tau, versus the reverse in LMW and HT7 immunodepleted fractions.

See also Figures S3, S4, S5, S6, and S7.

- MATLAB code to reproduce quantitative comparisons presented herein will be deposited at Zenodo (https://doi.org/10.5281/zenodo.15044381) and made publicly available as of the date of publication.
- Any additional information required to reanalyze the data reported in this paper will be available from the lead contact upon reasonable request.

ACKNOWLEDGMENTS

We thank UK DRI and UCL technical staff Elena Ghirardello and Phillip Muckett for the maintenance of animal colonies. We are grateful to Karen Duff for the kind provision of PS19 mice and controls. This work was supported by the UK Dementia Research Institute through UK DRI Ltd. (UKDRI-1208), principally funded by the UK Medical Research Council (M.A.B.). M.A.B. is further supported by a UKRI Future Leaders Fellowship (MR/X011038/1). M.A.B. and S.S.H. are further supported by the Cure Alzheimer's Fund. We gratefully acknowledge the donors of Alzheimer's Disease Research, a program of BrightFocus Foundation, for support contributing to this research (A2019112S, M.A.B.). S.S.H. is further supported by an Alzheimer's Association International Research Fellowship (AARF-23-1149637). F.W. is supported by the Deutsche Forschungsgemeinschaft (DFG, German Research Foundation), under Germany's Excellence Strategy – EXC 2067/1- 390729940; by the DFG – project-ID 317475864 – SFB 1286; by the DFG – project-ID 454648639 – SFB 1528; and by the Niedersächsisches Vorab of the VolkswagenStiftung through the Göttingen Campus Institute for Dynamics of Biological Networks (ZN3326 and ZN3371). F.W. further acknowledges support by the Max Planck Society and the Center for Biostructural Imaging of Neurodegeneration, Göttingen, Germany. A.N. and F.W. are supported by the DFG project-ID 436260547, in relation to NeuroNex (NSF 2015276). The Max Planck UCL Centre for Computational Psychiatry and Ageing Research is funded by the Max Planck Society (R.J.D.). B.T.H. is supported by the NIH (P30AG062421), Rainwater Foundation, Cure Alzheimer's Fund, and JPB Foundation. D. Dupret is funded by the Medical Research Council UK (MRC) (Programmes MC_UU_12024/3, MC_UU_00003/4, and MR/W004860/1). A. K. is a Hertie Senior Professor supported by DFG grant KO 979/7-1.

AUTHOR CONTRIBUTIONS

Conceptualization, S.S.H. and M.A.B.; methodology, S.S.H., R.E., J.H., D. Dasgupta, M.K., R.M.R., D.G., N.Q., D.S., C.C., Z.F., S.A.B., and M.A.B.; investigation, S.S.H., R.E., J.H., D. Dasgupta, M.K., R.M.R., D.G., N.Q., D. S., C.C., Z.F., and S.A.B.; visualization, S.S.H. and M.A.B.; funding acquisition, S.S.H., B.T.H., and M.A.B.; project administration, S.S.H. and M.A.B.; supervision, S.S.H., R.M.R., F.W., D. Dupret, R.J.D., A.K., A.N., B.T.H., and M.A.B.; writing – original draft, S.S.H. and M.A.B.; and writing – review and editing, all authors.

DECLARATION OF INTERESTS

B.T.H. owns stock in Novartis; he serves on the scientific advisory board of Dewpoint and has an option for stock. He serves on a scientific advisory board or is a consultant for AbbVie, Alexion, Ambagon, Aprinoia Therapeutics, Arvinas, Avrobio, AstraZeneca, Biogen, BMS, Cure Alz Fund, Cell Signalling, Dewpoint, Latus, Novartis, Pfizer, Sanofi, Sofinnova, Vigil, Violet, Voyager, and WaveBreak. His laboratory is in part supported by a sponsored research agreement from AbbVie. C.C. is currently employed at AbbVie.

STAR★METHODS

Detailed methods are provided in the online version of this paper and include the following:

- KEY RESOURCES TABLE
- EXPERIMENTAL MODEL AND STUDY PARTICIPANT DETAILS
  - Mice
  - Human Brain Tissue
  - Baculovirus system
  - E. Coli system
- METHOD DETAILS
  - *In vivo* Neuropixels experiments
  - Human brain tissue preparation and tau extraction
  - Recombinant tau protein expression/purification
  - Tissue Homogenization
  - HMW Tau Extraction
  - Tau Quantification by Western Blot
  - *In vitro* whole-cell patch clamp electrophysiology
  - *In vivo* whole-cell patch clamp electrophysiology
  - Immunohistochemistry, imaging, and analysis
- QUANTIFICATION AND STATISTICAL ANALYSIS

SUPPLEMENTAL INFORMATION

Supplemental information can be found online at https://doi.org/10.1016/j.cell.2025.04.006.

Received: October 17, 2024
Revised: February 21, 2025
Accepted: April 3, 2025
Published: April 28, 2025

REFERENCES

1. Dujardin, S., Commins, C., Lathuiliere, A., Beerepoot, P., Fernandes, A.R., Kamath, T.V., De Los Santos, M.B., Klickstein, N., Corjuc, D.L., Corjuc, B. T., et al. (2020). Tau molecular diversity contributes to clinical heterogeneity in Alzheimer's disease. Nat. Med. *26*, 1256–1263. https://doi.org/10.1038/s41591-020-0938-9.
2. Kim, C., Haldiman, T., Kang, S.G., Hromadkova, L., Han, Z.Z., Chen, W., Lissemore, F., Lerner, A., de Silva, R., Cohen, M.L., et al. (2022). Distinct populations of highly potent TAU seed conformers in rapidly progressing Alzheimer's disease. Sci. Transl. Med. *14*, eabg0253. https://doi.org/10.1126/scitranslmed.abg0253.
3. Busche, M.A., Wegmann, S., Dujardin, S., Commins, C., Schiantarelli, J., Klickstein, N., Kamath, T.V., Carlson, G.A., Nelken, I., and Hyman, B.T. (2019). Tau impairs neural circuits, dominating amyloid-β effects, in Alzheimer models in vivo. Nat. Neurosci. *22*, 57–64. https://doi.org/10.1038/s41593-018-0289-8.
4. Santacruz, K., Lewis, J., Spires, T., Paulson, J., Kotilinek, L., Ingelsson, M., Guimaraes, A., DeTure, M., Ramsden, M., McGowan, E., et al. (2005). Tau suppression in a neurodegenerative mouse model improves memory function. Science *309*, 476–481. https://doi.org/10.1126/science.1113694.
5. Harris, K.D., Hirase, H., Leinekugel, X., Henze, D.A., and Buzsáki, G. (2001). Temporal Interaction between Single Spikes and Complex Spike Bursts in Hippocampal Pyramidal Cells. Neuron *32*, 141–149. https://doi.org/10.1016/S0896-6273(01)00447-0.
6. Lowet, E., Sheehan, D.J., Chialva, U., De Oliveira Pena, R., Mount, R.A., Xiao, S., Zhou, S.L., Tseng, H.-A., Gritton, H., Shroff, S., et al. (2023). Theta and gamma rhythmic coding through two spike output modes in the hippocampus during spatial navigation. Cell Rep. *42*, 112906. https://doi.org/10.1016/j.celrep.2023.112906.
7. Ranck, J.B., Jr. (1973). Studies on single neurons in dorsal hippocampal formation and septum in unrestrained rats. I. Behavioral correlates and firing repertoires. Exp. Neurol. *41*, 461–531. https://doi.org/10.1016/0014-4886(73)90290-2.
8. Inglebert, Y., Aljadeff, J., Brunel, N., and Debanne, D. (2020). Synaptic plasticity rules with physiological calcium levels. Proc. Natl. Acad. Sci. USA *117*, 33639–33648. https://doi.org/10.1073/pnas.2013663117.
9. Payeur, A., Guerguiev, J., Zenke, F., Richards, B.A., and Naud, R. (2021). Burst-dependent synaptic plasticity can coordinate learning in hierarchical circuits. Nat. Neurosci. *24*, 1010–1019. https://doi.org/10.1038/s41593-021-00857-x.

10. Sjöström, P.J., Turrigiano, G.G., and Nelson, S.B. (2001). Rate, Timing, and Cooperativity Jointly Determine Cortical Synaptic Plasticity. Neuron *32*, 1149–1164. https://doi.org/10.1016/S0896-6273(01)00542-6.

11. Naud, R., and Sprekeler, H. (2018). Sparse bursts optimize information transmission in a multiplexed neural code. Proc. Natl. Acad. Sci. USA *115*, E6329–E6338. https://doi.org/10.1073/pnas.1720995115.

12. Doron, G., Shin, J.N., Takahashi, N., Drüke, M., Bocklisch, C., Skenderi, S., de Mont, L., Toumazou, M., Ledderose, J., Brecht, M., et al. (2020). Perirhinal input to neocortical layer 1 controls learning. Science *370*, eaaz3136. https://doi.org/10.1126/science.aaz3136.

13. Gava, G.P., McHugh, S.B., Lefèvre, L., Lopes-Dos-Santos, V., Trouche, S., El-Gaby, M., Schultz, S.R., and Dupret, D. (2021). Integrating new memories into the hippocampal network activity space. Nat. Neurosci. *24*, 326–330. https://doi.org/10.1038/s41593-021-00804-w.

14. Li, R., Huang, J., Li, L., Zhao, Z., Liang, S., Liang, S., Wang, M., Liao, X., Lyu, J., Zhou, Z., et al. (2023). Holistic bursting cells store long-term memory in auditory cortex. Nat. Commun. *14*, 8090. https://doi.org/10.1038/s41467-023-43620-5.

15. Xu, W., Morishita, W., Buckmaster, P.S., Pang, Z.P., Malenka, R.C., and Südhof, T.C. (2012). Distinct neuronal coding schemes in memory revealed by selective erasure of fast synchronous synaptic transmission. Neuron *73*, 990–1001. https://doi.org/10.1016/j.neuron.2011.12.036.

16. Bittner, K.C., Grienberger, C., Vaidya, S.P., Milstein, A.D., Macklin, J.J., Suh, J., Tonegawa, S., and Magee, J.C. (2015). Conjunctive input processing drives feature selectivity in hippocampal CA1 neurons. Nat. Neurosci. *18*, 1133–1142. https://doi.org/10.1038/nn.4062.

17. Epsztein, J., Brecht, M., and Lee, A.K. (2011). Intracellular determinants of hippocampal CA1 place and silent cell activity in a novel environment. Neuron *70*, 109–120. https://doi.org/10.1016/j.neuron.2011.03.006.

18. O'Keefe, J., and Recce, M.L. (1993). Phase relationship between hippocampal place units and the EEG theta rhythm. Hippocampus *3*, 317–330. https://doi.org/10.1002/hipo.450030307.

19. Hunt, D.L., Linaro, D., Si, B., Romani, S., and Spruston, N. (2018). A novel pyramidal cell type promotes sharp-wave synchronization in the hippocampus. Nat. Neurosci. *21*, 985–995. https://doi.org/10.1038/s41593-018-0172-7.

20. Buzsáki, G. (2015). Hippocampal sharp wave-ripple: A cognitive biomarker for episodic memory and planning. Hippocampus *25*, 1073–1188. https://doi.org/10.1002/hipo.22488.

21. Bennett, R.E., DeVos, S.L., Dujardin, S., Corjuc, B., Gor, R., Gonzalez, J., Roe, A.D., Frosch, M.P., Pitstick, R., Carlson, G.A., et al. (2017). Enhanced Tau Aggregation in the Presence of Amyloid β. Am. J. Pathol. *187*, 1601–1612. https://doi.org/10.1016/j.ajpath.2017.03.011.

22. Mizuseki, K., Royer, S., Diba, K., and Buzsáki, G. (2012). Activity dynamics and behavioral correlates of CA3 and CA1 hippocampal pyramidal neurons. Hippocampus *22*, 1659–1680. https://doi.org/10.1002/hipo.22002.

23. Mizuseki, K., and Buzsáki, G. (2013). Preconfigured, skewed distribution of firing rates in the hippocampus and entorhinal cortex. Cell Rep. *4*, 1010–1021. https://doi.org/10.1016/j.celrep.2013.07.039.

24. Marinković, P., Blumenstock, S., Goltstein, P.M., Korzhova, V., Peters, F., Knebl, A., and Herms, J. (2019). In vivo imaging reveals reduced activity of neuronal circuits in a mouse tauopathy model. Brain *142*, 1051–1062. https://doi.org/10.1093/brain/awz035.

25. Girardeau, G., Benchenane, K., Wiener, S.I., Buzsáki, G., and Zugaro, M.B. (2009). Selective suppression of hippocampal ripples impairs spatial memory. Nat. Neurosci. *12*, 1222–1223. https://doi.org/10.1038/nn.2384.

26. van de Ven, G.M., Trouche, S., McNamara, C.G., Allen, K., and Dupret, D. (2016). Hippocampal Offline Reactivation Consolidates Recently Formed Cell Assembly Patterns during Sharp Wave-Ripples. Neuron *92*, 968–974. https://doi.org/10.1016/j.neuron.2016.10.020.

27. Lee, H., Wang, S., and Hudetz, A.G. (2020). State-Dependent Cortical Unit Activity Reflects Dynamic Brain State Transitions in Anesthesia. J. Neurosci. *40*, 9440–9454. https://doi.org/10.1523/JNEUROSCI.0601-20.2020.

28. Grienberger, C., Chen, X., and Konnerth, A. (2014). NMDA receptor-dependent multidendrite Ca(2+) spikes required for hippocampal burst firing in vivo. Neuron *81*, 1274–1281. https://doi.org/10.1016/j.neuron.2014.01.014.

29. Yoshiyama, Y., Higuchi, M., Zhang, B., Huang, S.M., Iwata, N., Saido, T.C., Maeda, J., Suhara, T., Trojanowski, J.Q., and Lee, V.M.Y. (2007). Synapse loss and microglial activation precede tangles in a P301S tauopathy mouse model. Neuron *53*, 337–351. https://doi.org/10.1016/j.neuron.2007.01.010.

30. Apostolides, P.F., Milstein, A.D., Grienberger, C., Bittner, K.C., and Magee, J.C. (2016). Axonal Filtering Allows Reliable Output during Dendritic Plateau-Driven Complex Spiking in CA1 Neurons. Neuron *89*, 770–783. https://doi.org/10.1016/j.neuron.2015.12.040.

31. Goodman, M.S., Kumar, S., Zomorrodi, R., Ghazala, Z., Cheam, A.S.M., Barr, M.S., Daskalakis, Z.J., Blumberger, D.M., Fischer, C., Flint, A., et al. (2018). Theta-Gamma Coupling and Working Memory in Alzheimer's Dementia and Mild Cognitive Impairment. Front. Aging Neurosci. *10*, 101. https://doi.org/10.3389/fnagi.2018.00101.

32. Rutishauser, U., Ross, I.B., Mamelak, A.N., and Schuman, E.M. (2010). Human memory strength is predicted by theta-frequency phase-locking of single neurons. Nature *464*, 903–907. https://doi.org/10.1038/nature08860.

33. Axmacher, N., Henseler, M.M., Jensen, O., Weinreich, I., Elger, C.E., and Fell, J. (2010). Cross-frequency coupling supports multi-item working memory in the human hippocampus. Proc. Natl. Acad. Sci. USA *107*, 3228–3233. https://doi.org/10.1073/pnas.0911531107.

34. Buzsáki, G., and Moser, E.I. (2013). Memory, navigation and theta rhythm in the hippocampal-entorhinal system. Nat. Neurosci. *16*, 130–138. https://doi.org/10.1038/nn.3304.

35. Grienberger, C., and Magee, J.C. (2022). Entorhinal cortex directs learning-related changes in CA1 representations. Nature *611*, 554–562. https://doi.org/10.1038/s41586-022-05378-6.

36. Takahashi, H., and Magee, J.C. (2009). Pathway interactions and synaptic plasticity in the dendritic tuft regions of CA1 pyramidal neurons. Neuron *62*, 102–111. https://doi.org/10.1016/j.neuron.2009.03.007.

37. Metz, A.E., Jarsky, T., Martina, M., and Spruston, N. (2005). R-type calcium channels contribute to afterdepolarization and bursting in hippocampal CA1 pyramidal neurons. J. Neurosci. *25*, 5763–5773. https://doi.org/10.1523/JNEUROSCI.0624-05.2005.

38. DeVos, S.L., Corjuc, B.T., Commins, C., Dujardin, S., Bannon, R.N., Corjuc, D., Moore, B.D., Bennett, R.E., Jorfi, M., Gonzales, J.A., et al. (2018). Tau reduction in the presence of amyloid-β prevents tau pathology and neuronal death in vivo. Brain *141*, 2194–2212. https://doi.org/10.1093/brain/awy117.

39. DeVos, S.L., Miller, R.L., Schoch, K.M., Holmes, B.B., Kebodeaux, C.S., Wegener, A.J., Chen, G., Shen, T., Tran, H., Nichols, B., et al. (2017). Tau reduction prevents neuronal loss and reverses pathological tau deposition and seeding in mice with tauopathy. Sci. Transl. Med. *9*, eaag0481. https://doi.org/10.1126/scitranslmed.aag0481.

40. Takeda, S., Wegmann, S., Cho, H., DeVos, S.L., Commins, C., Roe, A.D., Nicholls, S.B., Carlson, G.A., Pitstick, R., Nobuhara, C.K., et al. (2015). Neuronal uptake and propagation of a rare phosphorylated high-molecular-weight tau derived from Alzheimer's disease brain. Nat. Commun. *6*, 8490. https://doi.org/10.1038/ncomms9490.

41. Kumar, M., Quittot, N., Dujardin, S., Schlaffner, C.N., Viode, A., Wiedmer, A., Beerepoot, P., Chun, J.E., Glynn, C., Fernandes, A.R., et al. (2024). Alzheimer proteopathic tau seeds are biochemically a forme fruste of mature paired helical filaments. Brain *147*, 637–648. https://doi.org/10.1093/brain/awad378.

42. Mate De Gerando, A., Welikovitch, L.A., Khasnavis, A., Commins, C., Glynn, C., Chun, J.E., Perbet, R., and Hyman, B.T. (2023). Tau seeding and spreading in vivo is supported by both AD-derived fibrillar and oligomeric tau. Acta Neuropathol. *146*, 191–210. https://doi.org/10.1007/s00401-023-02600-1.

43. Bancher, C., Brunner, C., Lassmann, H., Budka, H., Jellinger, K., Wiche, G., Seitelberger, F., Grundke-Iqbal, I., Iqbal, K., and Wisniewski, H.M. (1989). Accumulation of abnormally phosphorylated tau precedes the formation of neurofibrillary tangles in Alzheimer's disease. Brain Res. *477*, 90–99. https://doi.org/10.1016/0006-8993(89)91396-6.

44. Hill, E., Karikari, T.K., Moffat, K.G., Richardson, M.J.E., and Wall, M.J. (2019). Introduction of Tau Oligomers into Cortical Neurons Alters Action Potential Dynamics and Disrupts Synaptic Transmission and Plasticity. eNeuro *6*, ENEURO.0166-19.2019. https://doi.org/10.1523/ENEURO.0166-19.2019.

45. Wegmann, S., Eftekharzadeh, B., Tepper, K., Zoltowska, K.M., Bennett, R. E., Dujardin, S., Laskowski, P.R., MacKenzie, D., Kamath, T., Commins, C., et al. (2018). Tau protein liquid-liquid phase separation can initiate tau aggregation. EMBO J. *37*, e98049. https://doi.org/10.15252/embj.201798049.

46. Fukumoto, H., Kao, T.H., Tai, C.Y., Jang, M.K., and Miyamoto, M. (2024). High-molecular-weight oligomer tau (HMWoTau) species are dramatically increased in Braak-stage dependent manner in the frontal lobe of human brains, demonstrated by a novel oligomer Tau ELISA with a mouse monoclonal antibody (APNmAb005). FASEB J. *38*, e70160. https://doi.org/10.1096/fj.202401704R.

47. Bittner, K.C., Milstein, A.D., Grienberger, C., Romani, S., and Magee, J.C. (2017). Behavioral time scale synaptic plasticity underlies CA1 place fields. Science *357*, 1033–1036. https://doi.org/10.1126/science.aan3846.

48. Dorian, C.C., Taxidis, J., Arac, A., and Golshani, P. (2024). Behavioral timescale synaptic plasticity in the hippocampus creates non-spatial representations during learning and is modulated by entorhinal inputs. Preprint at bioRxiv. https://doi.org/10.1101/2024.08.27.609983.

49. Pettit, N.L., Yap, E.L., Greenberg, M.E., and Harvey, C.D. (2022). Fos ensembles encode and shape stable spatial maps in the hippocampus. Nature *609*, 327–334. https://doi.org/10.1038/s41586-022-05113-1.

50. Tanaka, K.Z., He, H., Tomar, A., Niisato, K., Huang, A.J.Y., and McHugh, T. J. (2018). The hippocampal engram maps experience but not place. Science *361*, 392–397. https://doi.org/10.1126/science.aat5397.

51. Harrison, T.M., Maass, A., Adams, J.N., Du, R., Baker, S.L., and Jagust, W. J. (2019). Tau deposition is associated with functional isolation of the hippocampus in aging. Nat. Commun. *10*, 4900. https://doi.org/10.1038/s41467-019-12921-z.

52. Styr, B., and Slutsky, I. (2018). Imbalance between firing homeostasis and synaptic plasticity drives early-phase Alzheimer's disease. Nat. Neurosci. *21*, 463–473. https://doi.org/10.1038/s41593-018-0080-x.

53. Wiegand, J.P., Gray, D.T., Schimanski, L.A., Lipa, P., Barnes, C.A., and Cowen, S.L. (2016). Age Is Associated with Reduced Sharp-Wave Ripple Frequency and Altered Patterns of Neuronal Variability. J. Neurosci. Off. J. Soc. Neurosci. *36*, 5650–5660. https://doi.org/10.1523/jneurosci.3069-15.2016.

54. Harris, S.S., Wolf, F., De Strooper, B., and Busche, M.A. (2020). Tipping the Scales: Peptide-Dependent Dysregulation of Neural Circuit Dynamics in Alzheimer's Disease. Neuron *107*, 417–435. https://doi.org/10.1016/j.neuron.2020.06.005.

55. Mate de Gerando, A., Khasnavis, A., Welikovitch, L.A., Bhavsar, H., Glynn, C., Quittot, N., Perbet, R., and Hyman, B.T. (2024). Aqueous extractable nonfibrillar and sarkosyl extractable fibrillar Alzheimer's disease tau seeds have distinct properties. Acta Neuropathol. Commun. *12*, 145. https://doi.org/10.1186/s40478-024-01849-1.

56. Schneider, C.A., Rasband, W.S., and Eliceiri, K.W. (2012). NIH Image to ImageJ: 25 years of image analysis. Nat. Methods *9*, 671–675. https://doi.org/10.1038/nmeth.2089.

57. Pachitariu, M., Shashwat, S., and Carsen, S. (2023). Solving the spike sorting problem with Kilosort. Preprint at bioRxiv. https://doi.org/10.1101/2023.01.07.523036.

58. Tort, A.B.L., Kramer, M.A., Thorn, C., Gibson, D.J., Kubota, Y., Graybiel, A. M., and Kopell, N.J. (2008). Dynamic cross-frequency couplings of local field potential oscillations in rat striatum and hippocampus during performance of a T-maze task. Proc. Natl. Acad. Sci. USA *105*, 20517–20522. https://doi.org/10.1073/pnas.0810524105.

59. Oakley, D.H., Chung, M., Abrha, S., Hyman, B.T., and Frosch, M.P. (2024). β-Amyloid species production and tau phosphorylation in iPSC-neurons with reference to neuropathologically characterized matched donor brains. J. Neuropathol. Exp. Neurol. *83*, 772–782. https://doi.org/10.1093/jnen/nlae053.

60. Tepper, K., Biernat, J., Kumar, S., Wegmann, S., Timm, T., Hübschmann, S., Redecke, L., Mandelkow, E.M., Müller, D.J., and Mandelkow, E. (2014). Oligomer formation of tau protein hyperphosphorylated in cells. J. Biol. Chem. *289*, 34389–34407. https://doi.org/10.1074/jbc.M114.611368.

61. Glynn, C., Chun, J.E., Donahue, C.C., Nadler, M.J.S., Fan, Z., and Hyman, B.T. (2024). Reconstitution of the Alzheimer's Disease Tau Core Structure from Recombinant Tau(297–391) Yields Variable Quaternary Structures as Seen by Negative Stain and Cryo-EM. Biochemistry *63*, 194–201. https://doi.org/10.1021/acs.biochem.3c00425.

62. Jun, J.J., Steinmetz, N.A., Siegle, J.H., Denman, D.J., Bauza, M., Barbarits, B., Lee, A.K., Anastassiou, C.A., Andrei, A., Aydın, Ç., et al. (2017). Fully integrated silicon probes for high-density recording of neural activity. Nature *551*, 232–236. https://doi.org/10.1038/nature24636.

63. Nitzan, N., McKenzie, S., Beed, P., English, D.F., Oldani, S., Tukker, J.J., Buzsáki, G., and Schmitz, D. (2020). Propagation of hippocampal ripples to the neocortex by way of a subiculum-retrosplenial pathway. Nat. Commun. *11*, 1947. https://doi.org/10.1038/s41467-020-15787-8.

64. Nitzan, N., Swanson, R., Schmitz, D., and Buzsáki, G. (2022). Brain-wide interactions during hippocampal sharp wave ripples. Proc. Natl. Acad. Sci. USA *119*, e2200931119. https://doi.org/10.1073/pnas.2200931119.

65. Perbet, R., Mate de Gerando, A., Glynn, C., Donahue, C., Gaona, A., Taddei, R.N., Gomez-Isla, T., Lathuiliere, A., and Hyman, B.T. (2024). In situ seeding assay: A novel technique for direct tissue localization of bioactive tau. J. Neuropathol. Exp. Neurol. *83*, 870–881. https://doi.org/10.1093/jnen/nlae059.

66. Oliva, C., Cohen, I.S., and Mathias, R.T. (1988). Calculation of time constants for intracellular diffusion in whole cell patch clamp configuration. Biophys. J. *54*, 791–799. https://doi.org/10.1016/S0006-3495(88)83017-0.

67. Barger, N., Sheley, M.F., and Schumann, C.M. (2015). Stereological study of pyramidal neurons in the human superior temporal gyrus from childhood to adulthood. J. Comp. Neurol. *523*, 1054–1072. https://doi.org/10.1002/cne.23707.

68. Evans, R., Dal Poggetto, G., Nilsson, M., and Morris, G.A. (2018). Improving the Interpretation of Small Molecule Diffusion Coefficients. Anal. Chem. *90*, 3987–3994. https://doi.org/10.1021/acs.analchem.7b05032.

69. Dasgupta, D., Warner, T.P.A., Erskine, A., and Schaefer, A.T. (2022). Coupling of mouse olfactory bulb projection neurons to fluctuating odour pulses. J. Neurosci. *42*, 4278–4296. https://doi.org/10.1523/JNEUROSCI.1422-21.2022.

70. Ackels, T., Erskine, A., Dasgupta, D., Marin, A.C., Warner, T.P.A., Tootoonian, S., Fukunaga, I., Harris, J.J., and Schaefer, A.T. (2021). Fast odour

dynamics are encoded in the olfactory system and guide behaviour. Nature *593*, 558–563. https://doi.org/10.1038/s41586-021-03514-2.

71. Margrie, T.W., Brecht, M., and Sakmann, B. (2002). In vivo, low-resistance, whole-cell recordings from neurons in the anaesthetized and awake mammalian brain. Pflugers Arch. *444*, 491–498. https://doi.org/10.1007/s00424-002-0831-z.

72. Margrie, T.W., and Schaefer, A.T. (2003). Theta oscillation coupled spike latencies yield computational vigour in a mammalian sensory system. J. Physiol. *546*, 363–374. https://doi.org/10.1113/jphysiol.2002.031245.

73. Jordan, R. (2021). Optimized protocol for in vivo whole-cell recordings in head-fixed, awake behaving mice. Star Protoc. *2*, 100347. https://doi.org/10.1016/j.xpro.2021.100347.

STAR★METHODS

KEY RESOURCES TABLE

REAGENT or RESOURCE	SOURCE	IDENTIFIER
Antibodies		
Tau-13	BioLegend	Cat#: 835201; RRID:AB_2565341
GluN1 (NR1)	Synaptic Systems	Cat#: 114 103; RRID:AB_2112011
NeuN	Millipore	Cat#: MAB377; RRID:AB_2298772
Cav2.3 [CACNA1E]	Proteintech	Cat#: 27225-1-AP; RRID:AB_2880808
Goat anti-Mouse Alexa Fluor 594	Invitrogen	Cat#: A11005; RRID:AB_2534073
Goat anti-Mouse Alexa Fluor 647	Invitrogen	Cat#: A21235; RRID:AB_2535804
Goat anti-Rabbit Alexa Fluor 594	Invitrogen	Cat#: A11012; RRID:AB_2534079
Goat anti-Rabbit Alexa Fluor 647	Invitrogen	Cat#: A21245; RRID:AB_2535813
Tau Mouse Monoclonal Antibody (HT7)	ThermoFisher Scientific	Cat#: MN1000; RRID:AB_2314654
GAPDH Rabbit Monoclonal Antibody (14C10)	Cell Signaling Technology	Cat#: 2118; RRID:AB_561053
Tau Rabbit Polyclonal Antibody (DAKO)	Agilent	Cat#: A0024 (discontinued); RRID:AB_10013724
IRDye® 800CW Donkey anti-Mouse IgG Secondary Antibody	Licor	Cat#: 926-32212; RRID:AB_621847
IRDye® 800CW Donkey anti-Rabbit IgG Secondary Antibody	Licor	Cat#: 926-32213; RRID:AB_621848
Bacterial and virus strains		
E. coli BL21(DE3)	ThermoFisher Scientific	Cat#: EC0114
Biological samples		
Human brain frontal cortex region BA8/9	Brain bank from Massachusetts Alzheimer's Disease Research Center	https://www.madrc.org/
Chemicals, peptides, and recombinant proteins		
$KMeSO_3$	Sigma, Merck	Cat#: 83000-5G-F
HEPES	Sigma, Merck	Cat#: H3375-100G
KCl	Sigma, Merck	Cat#: P9333-500G
EGTA	Sigma, Merck	Cat#: E0396-10G
ATP-Na	Sigma, Merck	Cat#: A2383-1G
ATP-Mg	Sigma, Merck	Cat#: A9187-500MG
GTP-Na	Sigma, Merck	Cat#: G8877-25MG
Biocytin	Sigma, Merck	Cat#: B1758-50mg
NaCl	Sigma, Merck	Cat#: 71376-1KG
$MgCl_2$	Sigma, Merck	Cat#: M1028-100ML
$CaCl_2$	Sigma, Merck	Cat#: 21115-100ML
Bicuculline	Enzo Life Sciences	Cat#: ALX-550-515
Picrotoxin	Sigma, Merck	Cat#: P1675
Glutathione Monoethyl Ester	Santa Cruz	Cat#: sc-203974
Thiourea	Sigma, Merck	Cat#: T8656
Tau441, recombinant human	Millipore Sigma	Cat#: AG960
Protease/Phosphatase inhibitor cocktail	Cell Signaling Technology	Cat#: 5872
Benzamidine	Acros Organics	Cat#: 401790250
PMSF	Sigma	Cat#: 93482
TCEP	ThermoFisher Scientific	Cat#: 20491
Benzonase	Sigma	Cat#: E1014

(*Continued on next page*)

Continued

REAGENT or RESOURCE	SOURCE	IDENTIFIER
Halt Protease and Phosphatase Inhibitor cocktail	ThermoFisher Scientific	Cat#: 78446
IPTG	Teknova	Cat#: 13431
Imidazole	Sigma	Cat#: 8.14223
HisTrap column	Cytiva	Cat#: 17524802
Superloop injector/connector	Cytiva	Cat#: 18111382
Bis-Tris gel	Invitrogen	Cat#: NP0316BOX
MOPs SDS Running Buffer	Invitrogen	Cat#: NP0001-02
SimplyBlue Safe Stain	Invitrogen	Cat#: 445034
3C protease	ThermoFisher Scientific	Cat#: 88947
Ni-NTA agarose	Qiagen	Cat#: 30210
Amicon Ultra-15 30K	Merck Millipore	Cat#: UFC903024
1X NuPAGE LDS sample buffer	ThermoFisher Scientific	Cat#: NP0007
1X NuPAGE sample reducing agent	ThermoFisher Scientific	Cat#: NP0009
NuPAGE 4–12% Tris/Bis gel	ThermoFisher Scientific	Cat#: NP0323BOX
NuPAGE MOPS running buffer	ThermoFisher Scientific	Cat#: NP0001
iBlot™ 2 Transfer Stacks, nitrocellulose, regular size	ThermoFisher Scientific	Cat#: IB23001
iBlot™ 2 Transfer Stacks, PVDF, regular size	ThermoFisher Scientific	Cat#: IB24001
Intercept antibody diluent	Licor	Cat#: 927-65001
Intercept blocking buffer	Licor	Cat#: 927-60001
Streptavidin Alexa Fluor 488	Invitrogen	Cat#: S11223
Critical commercial assays		
Dynabeads Protein G	Life Technologies	Cat#: 10003D
Deposited data		
Source data for reproducing quantitative comparisons	This paper	Zenodo: https://doi.org/10.5281/zenodo.15044305
Experimental models: Cell lines		
Sf9	ThermoFisher Scientific	Cat#: 11496015
Experimental models: Organisms/strains		
B6.CgTg(APPswe,PSEN1dE9)85Dbo/Mmjax mice (APP/PS1)	Originally bought from MMRRC, bred in house	MMRRC Strain# 034832-JAX
B6.Cg-Tg(Camk2a-tTA)1Mmay/DboJ (CamK2-tTA)	Originally bought from Jax, bred in house	Jax Strain#: 007004
FVB-Fgf14Tg(tetO-MAPT*P301L)4510Kha/JlwsJ (Tg4510)	Originally bought from Jax, bred in house	Jax Strain#: 015815
B6;C3-Tg(Prnp-MAPT*P301S)PS19Vle/J (PS19)	Kind gift from Karen Duff, bred in house	Jax Strain #: 008169
C57BL/6	Charles River	C57BL/6NCrl
Recombinant DNA		
pET28a(+).his.3C.Tau2N4R	In house	N/A
Bacmid-his.Tev.Tau2N4R	In house	N/A
Software and algorithms		
MATLAB scripts for visualisation and statistical analyses of source data	This paper	Zenodo: https://doi.org/10.5281/zenodo.15044381
MATLAB 2024A	The MathWorks	https://se.mathworks.com/products/matlab.html
Image J	Schneider et al.[56]	https://imagej.nih.gov/ij/
Patchmaster	HEKA	https://www.heka.com/downloads/downloads_main.html#down_patchmaster

(*Continued on next page*)

Continued

REAGENT or RESOURCE	SOURCE	IDENTIFIER
Igor Pro 5	WaveMetrics	https://www.wavemetrics.com/software
SpikeGLX 3.0	GitHub	https://billkarsh.github.io/SpikeGLX/
pCLAMP 11	Molecular Devices	https://www.moleculardevices.com/products/axon-patch-clamp-system/acquisition-and-analysis-software/pclamp-software-suite
Kilosort 3	GitHub (Pachitariu et al.[57])	https://github.com/MouseLand/Kilosort (Version 4 now provided)
PHY	GitHub	https://github.com/cortex-lab/phy
Neuropixels Trajectory Explorer	GitHub	https://github.com/petersaj/neuropixels_trajectory_explorer
ModIndex_v2.m	GitHub (Tort et al.[58])	(https://github.com/tortlab/phase-amplitude-coupling/blob/master/ModIndex_v2.m).
Other		
Custom rodent diet (+ 200mg/kg doxycycline hyclate)	Inotiv	Cat#: TD.00502
Borosilicate pipette capillaries for patch-clamp recordings	Sutter, USA	Cat#: BF-150-86-10
Superdex200 10/300GL	GE Healthcare	Cat#: 17-5175-01
Neuropixels 1.0 probes	IMEC	PRB_1_4_0480_1_C
Chameleon3 Behavioural camera	Point Grey	CM3-U3-13Y3M-CS

EXPERIMENTAL MODEL AND STUDY PARTICIPANT DETAILS

Mice

All surgical and experimental procedures were conducted in accordance with: 1) the Animals (Scientific Procedures) Act 1986, approved by the Animal Welfare and Ethical Review Body (AWERB) at University College London (UCL), and performed under an approved UK Home Office project license at UCL (UK); or 2) the policies established by institutional animal welfare guidelines of the government of Upper Bavaria and the Lower Saxony State Office for Consumer Protection and Food Safety, respectively (Germany). Mice were housed under a 12 h light/dark-cycle with access to standard food and water *ad libitum* in a temperature- and humidity-controlled specific pathogen free (SPF) facility. The experimental APP/PS1-rTg4510 line was generated as described previously.[3] Briefly, B6.CgTg(APPswe,PSEN1dE9)85Dbo/Mmjax mice (APP/PS1, MMRRC Strain#: 034832-JAX) were first crossed to B6.Cg-Tg(Camk2a-tTA)1Mmay/DboJ (CamK2-tTA, Jax Strain#: 007004). Subsequent APP/PS1$^{+/0}$; CamK2-tTa$^{+/0}$ progeny were then crossed with heterozygous FVB-Fgf14Tg(tetO-MAPT*P301L)4510Kha/JlwsJ (Tg4510$^{+/0}$, Jax Strain#: 015815) mice to generate APP/PS1$^{+/0}$;CamK2-tTA$^{+/0}$;rTg4510$^{+/0}$ triple heterozygotes and single/double transgenic animals. Mice were used at 3, 6 and 7-9 months of age. Age-matched littermates that either expressed no transgenic alleles or carried only the CamK2-tTA transgene were used as controls. 9–10-month-old PS19 (B6;C3-Tg(Prnp-MAPT*P301S)PS19Vle/J) transgenic mice (Jax Strain #: 008169, kind gift from Karen Duff) and aged matched C57BL/6 littermate controls were used for additional comparisons. An independent cohort of C57BL/6 wild-type mice at postnatal days P13 to P18 were additionally used for *in vitro* patch clamp experiments. Animals of both sexes were used in this study, with mixed-sex cohorts throughout, and randomly allocated to the experimental groups. All mice were group housed until surgical procedures and assays, with daily checks for clinical appearance. Following surgeries for awake Neuropixels experiments, mice were singly housed to prevent interference to the craniotomy chamber and head-fixation apparatus by cage-mates, and checked daily for clinical signs until recordings. All animals were healthy and immunocompetent, and housed in cages which included a papier mâché house, cardboard tubes, wooden chew sticks and soft nesting materials, which were replaced as needed. For animals undergoing doxycycline treatment, mice were given *ad libitum* access to chow containing 200 mg/kg doxycycline (Inotiv TD.00502, fresh diet was administered twice per week), following standard protocols.[3,4,38] Mice were placed on the doxycycline diet at 3 months of age and maintained under treatment until assessment (Neuropixels recordings and post-mortem immunochemistry) at approximately 6 months of age. All other animals were drug and procedure naïve prior to recordings/assays. Sample sizes were determined according to standards in the field and previously published research.

Human Brain Tissue

Human tissue was obtained from the Neuropathology Core of the Massachusetts Alzheimer Disease Research Center with approval from The Massachusetts General Hospital Institutional Review Board (#1999P009556), in accordance with the Declaration of

Helsinki, with consent obtained from next of kin at the time of death. AD tissue was from a single 84-year-old Caucasian male donor with Braak VI neurofibrillary tangles and Thal stage V amyloid deposits, APOE genotype 4/4, age of onset 74, and with no other concurrent pathology noted. Post-translational modifications (PTMs), seeding activity and other biochemical information pertaining to this patient have been previously described in detail in our previous publication (patient AD7 in Kumar et al.[41]). Control patient tissue was from a single 89-year-old Caucasian female at Braak stage I and Thal stage 0 at time of death, APOE genotype 3/3, with a primary neuropathologic diagnosis of healthy control, and a secondary neuropathologic diagnosis of cerebrovascular disease (previously investigated as patient 2380 in Oakley et al.[59]).

Baculovirus system

The recombinant tau protein expression using baculovirus was carried out by following a protocol described previously with slight modification.[60] Briefly, bacmid his.Tev.Tau2N4R was transfected into Sf9 insect cells (obtained from ThermoFisher Scientific, with documented lineage) to generate baculoviruses. Following two rounds of virus amplification, the proteins were expressed in Sf9 cells by infecting with the recombinant baculovirus at a multiplicity of infection of 1–5, typically in six T150 cell culture flasks containing 75% confluent Sf9 cells. Cells were incubated for 3 days at 27 °C and collected by centrifugation (5000 g /10 minutes).

E. Coli system

The protocol was followed as described previously with slight modifications.[61] A pET28a(+).his.3C.Tau2N4R plasmid was transformed into E. coli BL21(DE3) cells (obtained from ThermoFisher Scientific). Cells were grown at 37 °C with shaking at 220−230 rpm until an optical density at 600 nm (OD600) reached approximately 0.6. Protein overexpression was induced by the addition of 100 μg/mL IPTG, followed by 2 h of growth under the same conditions. Cells were harvested, snap-frozen, and stored at −80 °C until protein purification.

METHOD DETAILS

In vivo Neuropixels experiments

Surgical procedures

For all surgical procedures, general anesthesia was induced using ∼4% isoflurane in oxygen and maintained throughout the surgery at ∼2%. Anaesthetic depth was monitored via the pedal reflex and breathing rate. A subcutaneous injection of carprofen was provided pre-operatively for pain relief and ophthalmic gel (Viscotears) applied to protect the eyes during procedures. The scalp was first shaved, and the animal head fixed in a stereotaxic frame using ear bars. Body temperature was maintained at approximately 37 °C using a heating pad (WPI). The skin overlying the skull was disinfected with dilute chlorhexidine, cleaned with alcohol, and treated with topical application of lidocaine cream for 5 minutes before excision.

For Neuropixels recordings under anaesthesia, a small craniotomy was performed over the left parietal bone using a fine-tipped dental drill (OmniDrill35, WPI). A shallow indentation was drilled into the skull overlying the cerebellum, into which a silver chloride reference electrode was affixed using cyanoacrylate glue. A circular well encircling the exposed skull was then formed using dental cement (Lang). Animals were subsequently transferred directly to the recording rig with no interruption of anaesthesia.

For Neuropixels recordings performed in awake animals, the exposed skull was covered with Vetbond (3M), followed by a layer of Optical Adhesive 81 (Norland), which was cured by brief illuminations with a UV spot lamp (Intertronics). A craniotomy was performed as above. A custom-milled titanium plate was secured to the skull behind lambda using SuperBond dental cement (Prestige Dental) before a well was created with dental cement around the exposed skull as described above. Sterile phosphate-buffered-saline (PBS) was applied to the craniotomy before the entire well was sealed with KwikCast (World Precision Instruments). Following recovery from surgical procedures, animals received a subcutaneous buprenorphine injection for immediate pain relief and were provided with drinking water containing carprofen for 3 days postoperatively while body weight and clinical signs were monitored. Animals were allowed to recover for at least 1 week before their first habituation session (see below).

Neuropixels recordings

For recordings in awake animals, mice were habituated to handling procedures, head fixation apparatus and recording setup across three daily sessions or until the animal appeared comfortable with the experimenter and with the recording environment. During experiments, mice were head fixed above a rolling styrofoam wheel using the implanted headplate. Prior to probe implantation, mice were lightly sedated with isoflurane. The well was cleaned with alcohol using a cotton bud, allowed to dry, and the silicone plug carefully removed. Following inspection of the craniotomy, a silver chloride reference electrode was secured to the edge of the well, in contact with the skull, using dental cement (Lang).

A Neuropixels 1.0 probe[62] (IMEC) was secured to a QUAD micromanipulator (Sutter Instruments) and spatially referenced to bregma while orthogonal to the anterior posterior (AP) axis. The probe was then maneuvered to -2.3 mm AP -2 mm ML (60°) or -2.7 mm AP -2.5 mm ML (50°), and slowly inserted at a speed of ∼10 μm/s to a depth of ∼3.2 mm, thus traversing cortical and CA1 regions. Following implantation, anesthesia was either removed (for awake recordings) or gradually lowered to ∼1% (for anesthetized recordings). Recordings were not initiated until at least 35 minutes following probe implantation. Experimental sessions (2-3 awake, 1 anaesthetised) consisted of 10 min recordings of spontaneous brain activity sampled at ∼30 kHz (action potential data) and

2.5 kHz (LFP, local field potential data). Animals which underwent anaesthetised recordings were immediately sacrificed following experiments without recovery.

Awake recordings in darkness consisted of additional monitoring of the mouse's head and forelimbs using an infrared (IR) camera (Point Grey Chameleon3) and a rotary encoder attached to the running wheel to monitor locomotion. Rotary encoder data was converted to absolute rotations per minute (RPM), with stationary periods defined as timepoints where angular acceleration was < 0.025 RPM/sec and velocity was < 0.01 RPM. To identify non-locomotor movements such as blinking, grooming, and whisking, the rectified first approximate derivative of the mean intensity value was calculated across all pixels in each frame of IR camera videos. Non-locomotor movements were defined as signal crossings above 6-fold median absolute deviations. Recordings were then split into 2 second epochs, with any identified windows uninterrupted by locomotion or non-locomotor movements defined as resting state epochs, and those where locomotion was detected.

Neuropixels Analysis

Recordings were acquired using SpikeGLX software and processed using the Kilosort 3[57] automated spike sorting algorithm using default parameters. The brain regions traversed by each Neuropixels probe, and their position along the probe shank, were estimated by leveraging the experimental stereotactic coordinates (anterior-posterior, medial-lateral, micromanipulator azimuth and elevation) and a customised MATLAB script comprising of a modification to the open-source Neuropixels Trajectory Explorer with the Allen Common Coordinate Framework (CCF) version 3 mouse atlas (https://github.com/petersaj/neuropixels_trajectory_explorer) (GPL-3.0 License). This provided a predicted anatomical trajectory of the Neuropixels probe as a function of channel along the probe shank. Since probes were not fully implanted (~3200 μm), an offset to this trajectory vector was calculated by creating a depth template of probe channels, in which estimated cortical areas and CA1 regions were nominally set to a non-zero value with all other areas/channels set to zero. Thus, the depth template comprised of two square waves, reflecting the spread of cortical and CA1 regions according to the predicted trajectory, and separated by the intervening corpus callosum. We next extracted unit counts, as well as total power in the sharp wave ripple frequency band in the local field potential over time (SWR, 110-250 Hz, elevated in CA1), in order to yield a vector for unit incidence and SWR power across channels/depths, subsequently normalised between 0 and 1 and smoothed using a moving average filter. The product of both factors was then cross-correlated to the depth template, and the estimated offset between these given by the normalised cross-correlation possessing the largest absolute value (MATLAB function 'finddelay'). This offset was then used to align the predicted anatomical trajectory to functional data, and assign each neuron/unit to a putative brain-region (Figure S1A). Trajectory estimation was then visually confirmed for correspondence with predicted anatomical labels and adjusted manually if necessary. We next estimated the putative bounds of the CA1 pyramidal layer by nominally selecting 150μm either side of the SWR power peak, rounded to the nearest inflection point in the unit incidence depth profile (Figure S1A).

Spike waveforms associated with each identified neuron/unit were extracted, averaged across events, and normalised. The first and second principal components were computed for each waveform (MATLAB function 'pca') and used as inputs to generate a Gaussian mixture distribution model (GMM, MATLAB function 'fitgmdist', 200 replicates) for subsequent clustering with two components (MATLAB function 'cluster'), with the smallest cluster, consisting of artefactual signals, excluded from further analysis. Remaining waveforms were subsequently visually checked to confirm physiological appearance in PHY software (https://github.com/cortex-lab/phy), and their properties (width of the spike deflection and trough-to-peak time) used to cluster neurons/units into putative excitatory and inhibitory populations. This clustering was performed on collated units derived from the putative CA1 pyramidal layer region across animals from the same background for each state condition (i.e., awake or anesthetized), and consisted of a Gaussian mixture model (GMM) applied to the data using the iterative Expectation-Maximization (EM) algorithm (MATLAB function 'fitgmdist', 500 replicates, 500 iterations, 4 clusters). Putative fast-spiking inhibitory neurons were defined as those belonging to a distinct cluster associated with more brief (i.e., fastest) waveform dynamics (~10-20% of total units across awake and anesthetized experiments), while remaining units (with slower spike dynamics) were considered to be mostly comprised of putative excitatory pyramidal neurons (Figure 1C, right). In this study, we constrained our analysis to putative excitatory pyramidal neurons in hippocampus CA1.

Unit quality metrics

Neurons/units were considered to be well isolated and included for further analysis if they met the following criteria: amplitude cutoff < 0.1 ("unit completeness") and inter-spike-interval violations < 0.25 ("unit contamination").

Bursting analysis

Inter-spike-intervals (ISIs) between all spiking events *in-vivo* were computed and extracted for each unit/neuron, with burst spikes defined, unless otherwise stated, as those with ISIs < 10 ms (i.e., the intra-burst ISI threshold).[6] The burst index (i.e., the propensity for neurons to burst) was defined as the number of intra-burst ISIs divided by the total number of ISIs during the recording period; qualitatively similar results were obtained using intra-burst ISI thresholds ranging from 4-12 ms, similarly to that previously reported,[5,23] and are also presented when examining effects on faster and slower burst events (corresponding to smaller and larger intra-burst ISI thresholds, respectively).

Spike-LFP phase-locking value

In order to quantify the consistency of spiking activity relative to the phase of LFP oscillations, we calculated the phase-locking value (PLV) for each neuron/unit as a function of frequency:

$$PLV(f) = \left|\frac{1}{N}\right|\sum_{N} e^{i\phi(f,n)}$$

where f is frequency and N is the total number of spikes. The phase variable ϕ was computed from the complex wavelet spectrum[6] (MATLAB functions 'cwt' and 'angle') of the low-pass filtered and decimated LFP time-series (Chebyshev Type 1 IIR filter, Order = 8 filter, to 500 Hz sampling rate), taken from a vertically adjacent CA1-labelled channel (20 μm distance, to avoid possible spike artefacts).

Phase-amplitude coupling

Cross-frequency phase-amplitude coupling was computed using a continuous Morlet wavelet transform (MATLAB function 'cwt') for 'phase' frequencies 2-18 Hz (voices per octave = 20) and 'amplitude' frequencies 20-100 Hz (voices per octave = 14). This was applied to a single downsampled LFP timeseries for each animal, acquired from the CA1-associated channel which exhibited the greatest power in the ripple frequency range (110-250 Hz, MATLAB function 'bandpower') and which was presumed to colocalise with the CA1 pyramidal layer. Phase and amplitude signals (MATLAB function 'angle' and 'abs', respectively) were then extracted and the modulation index (MI) calculated to quantify amplitude modulation by phase by means of a normalised entropy measure[58] (https://github.com/tortlab/phase-amplitude-coupling/blob/master/ModIndex_v2.m).

Ripple oscillation detection and analysis

Local field potential data (sampling rate 2.5 kHz) were filtered for the ripple band (110 to 250 Hz; 4th order Butterworth filter with Second-Order-Section implementation for stability), and envelopes/instantaneous amplitudes calculated using the Hilbert transform (MATLAB functions 'hilbert' and 'abs'). Ripple events were detected similarly to previously published protocols.[13] Local maxima in the ripple band envelope which exceeded five times the median of the envelope values within that channel during quiescence were collated as candidate ripple events. Onset and offset for each event were defined as the nearest timepoints prior to and following local maxima in which ripple band envelope fell below 50% of the detection threshold, with ripple event time defined as the time of the local maxima. Candidate events were included for final analysis if ripple band power during the event was at least twice as large as that in the common average reference and that of the power in the supra-ripple band (200-500 Hz, to account for high frequency noise), occurred when the animal was quiescent and if the theta/delta power ratio was <2 (i.e. during the resting state), and if the event was at least 4 ripple cycles in length and separated from another by at least 500 ms. Similarly to previous protocols,[63,64] we next computed ripple triggered peri-event time histograms (PETHs) for each identified putative excitatory pyramidal neuron/unit by counting spiking activity in 10ms bins (between -1 to +1 s of the ripple peak time). PETHs for each neuron/unit within each experimental session were averaged across ripple events, converted to Hz, smoothed with a 50 ms Gaussian filter, and z-scored. The unit-related peak response within ±200 ms of the ripple onset time was extracted and, together with the PETH, averaged across neurons/units within each experimental session, then averaged across sessions to yield metrics at the individual animal level.

Human brain tissue preparation and tau extraction

Frozen human brain tissue was briefly thawed on wet ice followed by a grey matter dissection. Grey matter was dounce homogenized with 30 up and down strokes in five volumes (wt/vol) of cold PBS/1X protease/phosphatase inhibitors using a Teflon-glass homogenizer. The homogenate was centrifuged at 10,000 g for 10 min at 4 °C. Supernatants were collected, aliquoted, and stored at −80 °C before use.

Size Exclusion Chromatography and immunodepletion

Human brain soluble extracts were isolated by SEC as previously described[40] on a Superdex200 10/300GL columns (no. 17-5175-01, GE Healthcare) in PBS at a flow rate of 0.5 mL/min, with an AKTA purifier 10 (GE Healthcare). Briefly, each brain extract was loaded undiluted at a final volume of 0.5mL onto the SEC column. Fractions of 500 μL were retrieved and fractions 2, 3, 4 containing High Molecular Weight (HMW) tau were pooled, and fractions 13, 14, 15 containing Low Molecular Weight (LMW) tau were pooled. Tau immunodepletion was performed using Dynabeads Protein G for Immunoprecipitation (#10003D, Life Technologies) according to the manufacturer's instructions with minor modifications. The amount of 750 μg of Dynabeads Protein G were incubated with 5 μg of total tau antibody (HT7, #MN1000, Thermo Scientific) or random human control IgG for 10 minutes with rotation at RT. After washing with 100 μL PBS the bead-antibody complex was incubated with 100 μL of pooled HMW or LMW tau SEC fractions for 1 hour with rotation at RT. The bead-antibody-antigen complex was isolated using a magnetic holder and the supernatant was transferred to a clean tube.

Recombinant tau protein expression/purification

Baculovirus system

Cells containing phosphorylated Tau2N4R protein were resuspended in 30 mL lysis buffer (50 mM Tris-HCl, pH 7.3, 100 mM NaCl, 10% glycerol, 5mM imidazole) which was freshly supplemented with 1 mM Benzamidine, 0.1 mM PMSF, 0.5 mM TCEP, 30 U/mL Benzonase and Halt Protease and Phosphatase Inhibitor cocktail (Thermo Scientific). Subsequently, the cells were crushed once

in a French press. Next, lysed cells were boiled in a water bath at 100 °C for 20 min. The cell debris was removed by centrifuging the lysate for 15 min at 15,000 g, and the supernatant containing soluble tau was removed and filtered with a 0.22 μm syringe filter (Merck Millipore) and the pellet was discarded. The purification part is the same as with the E. coli tau purification method below.

E. Coli system

The cell pellet was resuspended in 30 mL lysis buffer (50 mM Tris-HCl pH: 7.3, 100 mM NaCl, 10% glycerol, 5 mM Imidazole with 0.1 mM PMSF, 0.5 mM TCEP) supplemented freshly with 30 U/mL Benzonase and Halt Protease Inhibitor cocktail (Thermo Scientific). The cells were lysed with two runs of French pressure lysis, boiled 20 min and centrifuged at 15,000 g for 30 min. The supernatant was removed and filtered with a 0.22 μm syringe filter (Merck Millipore) and the pellet was discarded. Then, roughly 30 mL of filtered supernatant was next injected over a 5 mL histrap column (Cytiva) attached to an ÄKTA Pure (Cytiva) using a 50 mL Superloop injector/connector (Cytiva). The sample was injected with 40 mL of binding buffer (50 mM sodium phosphate (pH: 7.2), 300 mM NaCl, 10 mM Imidazole supplemented with 1 mM Benzamidine and 0.5 mM TCEP). Next, the column was washed with 50 mL of wash buffer (50 mM sodium phosphate (pH:7.2), 300 mM NaCl, 25 mM Imidazole supplemented with 1 mM Benzamidine and 0.5 mM TCEP). The sample was eluted from the column using a linear gradient over 60 mL from binding buffer to an elution buffer (50 mM sodium phosphate (pH: 7.2), 300 mM NaCl, 1 mM Imidazole supplemented with 1 mM Benzamidine and 0.5 mM TCEP) with 2 mL fractions collected. Fractions with high ultraviolet (UV) signal were run on a 10% Bis-Tris gel (Invitrogen) in MOPs SDS Running Buffer (Invitrogen), followed by staining with SimplyBlue Safe Stain (Invitrogen). Fractions containing His.3C.Tau2N4R were pooled, and dialyzed 2x against PBS 4 °C, O/N followed by RT for 2 hrs. The his tag of the dialyzed protein was cleaved with 3C protease (Thermo fisher Scientific) 4 °C, O/N. The 3C protease was removed with Ni-NTA agarose (Qiagen) 4 °C 2 hrs. The cleaved protein was concentrated with Amicon Ultra-15 30K (Merck Millipore). Protein was aliquoted and flash-frozen for storage at −80 °C until further use.

Tissue Homogenization

Brain tissue was homogenized at a 5:1 volume to brain mass (g) ratio using phosphate buffer saline (PBS) supplemented with 1X protease/phosphatase inhibitor cocktail (5872 Cell Signaling Technology) in a 2 mL glass homogenizer with 30 up and down strokes on ice by hand. The homogenates were transferred to a 1.5 mL microcentrifuge tube and centrifuged at 10,000 g for 10 minutes at 4 °C. Supernatant from this centrifugation was reserved and stored at -80 °C until further use.

HMW Tau Extraction

HMW tau species were pelleted by ultracentrifugation as previously described.[41] Briefly, 200 μL from the supernatant of the homogenized tissue were centrifuged at 150,000 g for 30 min at 4 °C. Following ultracentrifugation, 180 μL of supernatant from this step was collected and stored at -80 °C as the LMW tau fraction. The remaining 20 μL was supplemented with an additional 20 μL of phosphate buffer saline (PBS) to resuspend the pellet. Resuspended pellets were stored at -80 °C as the HMW tau fraction.

Tau Quantification by Western Blot

Total tau quantity was evaluated by western blotting, as previously described[42,65] and equal protein concentration between the samples was confirmed using a BCA assay. Tissue-derived samples were diluted 1:10 in PBS and supplemented in 1X NuPAGE LDS sample buffer (Thermo Fisher) and 1X NuPAGE sample reducing agent (Thermo Fisher). Recombinant wildtype 2N4R tau (Tau441, AG960, Millipore) was prepared in the same way at the indicated concentrations. The prepared samples were then heated at 95 °C for 5 min and loaded onto a NuPAGE 4–12% Tris/Bis gel (Thermo Fisher). Gels were run in 1x NuPAGE MOPS running buffer (Thermo Fisher). Human derived proteins were transferred onto a PVDF membrane while mouse derived proteins were transferred onto nitrocellulose membrane using iBlot 2 gel transfer device for 7 min at 25 V (Thermo Fisher). Membranes were incubated for 1 hr at room temperature (RT) on rocking in Intercept blocking buffer (Licor). Following blocking, membranes were incubated on rocking overnight at 4 °C or 1 hr at room temperature with the anti-Tau HT7 (Invitrogen) diluted 1:1000, Dako anti-total Tau (Agilent) diluted 1:5000 in Intercept antibody diluent (Licor) or GAPDH (#2118, Cell Signalling Technology). Following these incubations, membranes were probed with the corresponding secondary antibody, donkey anti-mouse 800 (diluted 1:10,000) or donkey anti-rabbit 800 (diluted 1:5,000) diluted in Intercept antibody diluent (Licor) and imaged on a Licor Odyssey Clx. Images were exported from the Licor Odyssey Clx and analyzed using Fiji/ImageJ.[56] For quantification purposes, regions of interest were defined to encompass the entire signal within each lane, ensuring that the total tau amount was considered for each condition. Signal intensity was then measured using the area under the curve method.

In vitro whole-cell patch clamp electrophysiology

Acute hippocampal slice preparation

Mice were deeply anesthetized with CO_2 and decapitated, after which the brain was immediately removed and immersed in an ice-cold slicing solution containing (in mM) 24.7 glucose, 2.5 KCl, 65.47 NaCl, 26 $NaHCO_3$, 105 sucrose, 0.5 $CaCl_2$, 7 $MgCl_2$, 1.25 NaH_2PO_4, and 1.7 ascorbic acid (Fluka, Switzerland). The pH value was adjusted to 7.4 with HCl and stabilized by bubbling with carbogen, which contained 95% O_2 and 5% CO_2 and the osmolarity was 290-300 mOsm. 300 μm horizontal hippocampal slices were cut in the slicing solution using a vibratome (VT1200S; Leica, Germany). Brain slices were kept in the recovering solution which contained (in mM) 2 $CaCl_2$, 12.5 glucose, 2.5 KCl, 2 $MgSO_4$, 119 NaCl, 26 $NaHCO_3$, 1.25 NaH_2PO_4, 2 thiourea (Sigma, Germany), 5 Na-ascorbate (Sigma), 3 Na-pyruvate (Sigma), and either 1 glutathione monoethyl ester (Santa Cruz Biotechnology, U.S.A) or

N-acetyl-L-cysteine at 34 °C for a few minutes and after that at room temperature for at least one hour before the experiment. The pH value of the recovering solution was adjusted to 7.4 with HCl and constantly bubbled with carbogen, and the osmolarity was 290 mOsm.

Electrophysiological recordings

After recovering, individual hippocampal slices were transferred to the recording chamber, which was constantly perfused at a flow rate of 2 mL/min with artificial cerebrospinal fluid (ACSF) containing (in mM) 2 $CaCl_2$, 20 glucose, 4.5 KCl, 1 $MgCl_2$, 125 NaCl, 26 $NaHCO_3$, and 1.25 NaH_2PO_4 and gassed with 95% O_2 and 5% CO_2 to ensure oxygen saturation and to maintain a pH value of 7.4 at 30-32 °C. To block $GABA_AR$-mediated synaptic transmission, either 10 μM bicuculline (Enzo, U.S.A) or 30 μM picrotoxin (Sigma) were added to the ACSF. Somatic whole-cell recordings from CA1 pyramidal neurons were performed with a borosilicate glass pipette with a resistance of ca. 7 MΩ filled with an internal solution containing (in mM) 148 potassium gluconate, 10 HEPES, 10 NaCl, 0.5 MgCl2, 4 Mg-ATP and 0.4 Na3-GTP (pH 7.3). To study the effects of patient-derived tau on neuronal action potential firing, we added 0.1 nM, 1 nM, 10 nM HMW and 10 nM LMW tau to the pipette internal solution with appropriate dilutions based on calculated concentrations of HMW and LMW tau for each patient (Figure S3A), and using the average molecular weight for phospho-tau of 60 kDa (60,000 g/mol,[45]). Corresponding HT7 immunodepleted solutions were prepared in the same manner (i.e., to yield the same volumes) as those for different concentrations of HMW or LMW tau, and used as controls. When examining concentration dependent effects of HMW tau, we employed the corresponding HT7 immunodepleted solution prepared in the same manner (i.e., same volume) as the 0.1 nM HMW solution as our control. In turn, to study the effects of recombinant tau, we added 2 μM E.coli tau, 2 μM SF9 tau and 2 μM GAPDH (the latter as control). Additional control conditions included no addition to the pipette solution or only PBS. The pH value of the internal solutions was adjusted to 7.3 with KOH. Voltage- and current-clamp measurements were carried out using an EPC 9/2 patch-clamp amplifier (HEKA, Germany) in combination with the PULSE software (HEKA) for data acquisition and the generation of stimulation protocols. Alternatively, an EPC10 amplifier (HEKA) and the Patchmaster software (HEKA) were used for the same purposes. Data were visualized using Igor Pro (WaveMetrics). The membrane potential was held at -70 mV without liquid junction potential adjustment. Data were collected at 10 kHz and Bessel-filtered at 2.9 kHz.

Analysis

Data were imported into MATLAB and analysed using custom-written scripts. For each neuron, action potentials were identified, and inter-spike intervals (ISIs) at each consecutive current injection step (-50 pA, 100 pA, 200 pA, 300 pA, 400 pA) and series (each current step repeated seven times) were computed. Since *in vitro* patch clamp experiments consisted of current steps where bursts were invariably initiated at step onset, we quantified the number of individual single spikes and burst events (consisting of two or more spikes with ISIs < 10 ms) within the first 50 ms of each current step, and averaged over the seven current step repeats for each cell. We also examined the nature of the first event following the current step onset (no spikes, a single spike, or a burst event) and counted these across repeats for each current step. Only neurons that remained viable for the entire experimental protocol were included for analysis.

Confirmation of intracellular tau diffusion

To verify the entrance and diffusion of tau into the patched cells, pipettes were also loaded with 2.5 mg/mL biocytin. After completion of recordings, slices were fixed in PFA in PBS, and washed in PBS before being stored in PBS at 4 °C before immunolabelling. Slices were blocked in blocking solution (3% normal goat serum, 2% bovine serum albumin, 0.5% Triton in PBS) for 2 hours at room temperature (RT) before being incubated with Tau-13 primary antibody (1:1,000; BioLegend; 835201) in blocking solution for 40 hours at 4 °C. Slices were then warmed to RT and washed with PBS (10 minutes, then 3x1 hour) before incubation with secondary antibodies (Goat anti-mouse Alexa Fluor 594 [1:1,000; Invitrogen; A21235] and Streptavidin Alexa Fluor 488 [1:1,000; Invitrogen; S11223]) in blocking solution overnight at RT. Slices were then washed with PBS (10 minutes, then 3x 1 hour), labelled with DAPI, and mounted with ProLong Gold (Invitrogen). Images were subsequently acquired using a Zeiss LSM 980 confocal microscope using a 40x objective (field of view: 319.45 μm x 319.45 μm; 1024 x 1024 pixels) with a z-step size of 0.83 μm.

We estimated the time constant, τ, for intracellular diffusion of tau into patched cells using the following equation[66]:

$$\tau = \frac{VR}{D\rho}$$

where V is the estimated volume of a pyramidal soma (assumed 1.512×10^{-9} cm^3[67]), R is the measured pipette resistance (7 MΩ), D is the diffusion coefficient for tau and ρ is the resistivity of the pipette filling solution (assumed to be 100 Ω-cm, as previously[66]). We estimated the diffusion coefficient of tau, D, by exploiting a previously published Stokes-Einstein-Gierer-Wirtz Estimation (SEGWE) model implementation in MATLAB,[68] using 60 kDa as the standard molecular weight for phosphorylated tau, chamber temperature of 31 °C (304.15 K), and assuming, for simplicity, diffusion in water. Using this approach, we calculated D to be 8.7×10^{-7} cm^2/s, resulting in a time constant for tau diffusion of 122 seconds (time to 63.8% of asymptote value). Using this time constant we were able to generate a normalised diffusion curve describing diffusion of tau into the cell over time using the following equation (where t is time):

$$y(t) = 1 - e^{-\frac{t}{\tau}}$$

Under the reasonable assumption that $Volume_{pipette}$ (of the order of microlitres) >> $Volume_{soma}$, such that the pipette can be considered an infinite reservoir, we can estimate the intracellular tau concentration (C_{soma}) as:

$$C_{soma}(t) = C_{pipette}\left(1 - e^{-\frac{t}{\tau}}\right)$$

where $C_{pipette}$ is the initial tau concentration within the pipette. These estimates suggest that a significant amount of tau will have diffused into the cell by the time of the first recording, which typically took place approximately two minutes following cell breakthrough. For the case of 10 nM HMW tau concentration in the pipette, this would equate to an intracellular tau concentration of approximately 6 nM at the time of the first recording (Figure S4B, right).

In vivo whole-cell patch clamp electrophysiology

Surgery

Animals were weighed and anesthetized using a mixture of ketamine/xylazine (100 mg/kg and 10 mg/kg respectively) by intraperitoneal injection. Depth of anaesthesia was regularly monitored via the pedal reflex and breathing rate. The surgical site was shaved, and the skin cleaned with 1% chlorhexidine and alcohol. The anesthetized animal was then head-fixed in a stereotaxic frame (WPI) and placed on a heat-pad to maintain the body temperature, which was continuously monitored using a rectal probe. The scalp was incised and gently manipulated away from the skull with two arterial clamps on either side of the incision. A custom head-fixation implant was attached to the base of the skull with veterinary glue (Vetbond, 3M) such that its most anterior point rested approximately on lambda. Dental cement (Paladur, Heraeus Kulzer; Simplex Rapid Liquid, Associated Dental Products Ltd.) was then applied around the edges of the implant to ensure firm adhesion to the skull. A craniotomy over the right parietal bone (approximately ~2 mm diameter) was subsequently performed with a dental drill (OmniDrill35, WPI). The dura was then carefully removed using a bent 30G needle tip. Next, to access the dorsal hippocampus, an aspirator was used to aspirate the cortical tissue until the dorsal surface of the hippocampus could be visualized. To maintain stability of the tissue during the recordings, 10% (w/v) molten low melting point agarose (Merck) dissolved in ACSF (NaCl (125 mM), KCl (5 mM), HEPES (10 mM), pH adjusted to 7.4 with NaOH, $MgSO_4.7H_2O$ (2 mM), $CaCl_2.2H_2O$ (2 mM), glucose (10 mM)) with osmolarity ~300 mOsm/kg was applied to the area.

In vivo whole-cell recordings

Borosilicate pipettes (2x1.5 mm) were pulled and filled with (in mM) $KMeSO_3$ (130), HEPES (10), KCl (7), ATP-Na_2 (2), ATP-Mg (2), GTP-Na_x (0.5), EGTA (0.05) (pH = 7.3, osmolarity ~290 mOsm/kg). The brain surface was submerged with ACSF containing (in mM) NaCl (135), KCl (5.4), HEPES (5), $MgCl_2$ (1), $CaCl_2$ (1.8), (pH = 7.4 and ~300 mOsm/kg. Signals were amplified and low-pass filtered at 6 kHz using an Multiclamp 700B amplifier (Molecular Devices, USA) and digitized at 40 kHz using a Digidata 1550B (Molecular Devices, USA). Experimental steps were performed as described in previous publications.[69,70] Briefly, after zeroing the pipette tip position at the agar surface, we advanced the pipette tip until a sudden change in the offset potential was observed, typically at approximately 900-1200 μm depth. Next, we searched for a cell while stepping at 2 μm/s as described previously.[71–73] Upon a successful hit, we released the positive pressure to achieve a gigaseal. Subsequent gentle suction enabled whole-cell configuration after which we swiftly shifted to current-clamp mode to start a recording. Series resistance was compensated and monitored continuously during recordings. Neurons showing series resistance > 25 MΩ were discarded from further analysis. Data were visualised using pCLAMP software (Molecular Devices). Animals were sacrificed immediately following recordings without recovery.

Analysis

Data were imported into MATLAB and spontaneous spiking events extracted using custom-written scripts. For each neuron, inter-spike intervals (ISIs) were computed during stable spontaneous epochs (minimum 100 spikes in total) and burst index calculated as described above for Neuropixels experiments.

Immunohistochemistry, imaging, and analysis

Brains were extracted from animals after intracardiac perfusion of heparinised (10 U/ml; Sigma-Aldrich) 1x phosphate buffered saline (no calcium no magnesium; PBS; Gibco) followed by 4% paraformaldehyde (PFA) in PBS (Alfa Aesar), post-fixed for 24 hours in 4% PFA in PBS, cryopreserved through increasing sucrose concentrations, embedded in optimal cutting temperature compound (OCT; CellPath) and frozen on dry ice. 10 μm thick sagittal sections were cut using a Leica cryostat. Sections were blocked in blocking solution (10% goat serum, 0.3% triton in PBS) for 4 hours then incubated with GluN1 (NR1) (1:1,000; Synaptic Systems; 114 103), NeuN (1:500; Millipore; MAB377) and/or CaV2.3 (1:500; ProteinTech; 27225-1-AP) antibodies in block overnight at 4 °C. Sections were washed and incubated with secondary antibodies [Goat anti-Mouse Alexa Fluor 647 (1:500; Invitrogen; A21235), Goat anti-Rabbit Alexa Fluor 594 (1:1,000; Invitrogen; A11012), Goat anti-Rabbit Alexa Fluor 647 (1:500; Invitrogen; A21245)] in block for 2 hours at room temperature. Sections were then labelled with DAPI and mounted with ProLong Gold.

Immunolabelled sections were imaged on a Zeiss LSM980 confocal microscope using 63x magnification (field of view (FOV): 134.69 μm by 134.69 μm, 1024x1024 pixels). Analysis was carried out using the FIJI build of ImageJ (open source). CaV2.3: A total of 4-6 FOV containing the pyramidal layer of CA1 from 2-3 sections per animal were imaged (results averaged to give a single value per animal). One animal in which CA1 could not be imaged was excluded from further analysis. The pyramidal layer of CA1 was manually segmented, and a mask of neuronal soma was created using automated thresholding of NeuN staining. CaV2.3 staining was background corrected by thresholding, and the integrated density of staining was measured within the somatic mask. This was

then normalised to soma area. The experimenter was blinded to genotype prior to imaging and analysis. GluN1 (NR1): A total of 6-12 FOV containing the strata oriens and strata radiatum of CA1 from 2-3 sections per animal were imaged (results averaged to give a single value per animal). The strata oriens and strata radiatum were manually segmented and images were background corrected using rolling ball and automated thresholding, prior to automated quantification of the number of GluN1 (NR1) puncta. The experimenter was blinded to genotype prior to imaging and analysis.

QUANTIFICATION AND STATISTICAL ANALYSIS

Statistical testing consisted of parametric and non-parametric tests following Shapiro–Wilk or Kolmogorov-Smirnov tests for normality in MATLAB, with results considered significant at $p < 0.05$ (or $p < 0.1$ for interaction effects in two-way standard and mixed ANOVA tests). Statistical tests and the nature and number of biological units, definition of centre, dispersion and precision measures, as appropriate, are detailed in the associated figure legends. Linear regression models were fit using MATLAB function 'fitlm'. On two occasions, we aimed to examine the effect of genotype on neuronal bursting at the individual cell level while accounting for individual variability in mice. A linear mixed effects model was thus deployed (MATLAB function 'fitlme') with genotype as a fixed effect and mouse/subject identification code as a random effect. The model was specified as: BI $\sim$ genotype + (1|SubjectID), where BI denotes the burst index. Pairwise comparisons were subsequently conducted between multiple genotypes using the 'coefTest' function in MATLAB, with Bonferroni correction for multiple comparisons. We further conducted linear mixed effects modelling to examine the impact of baseline firing rates, genotype differences, and subject-specific variability on burst firing rates at the animal level, specified as: BurstFR $\sim$ BaselineFR + Genotype + (1|SubjectID). Data was log transformed where applicable. Repeated measures ANOVA tests were followed by Mauchly's test for sphericity (compound symmetry assumption, MATLAB function 'mauchly') and p-values lower-bound adjusted if required.

Supplemental figures

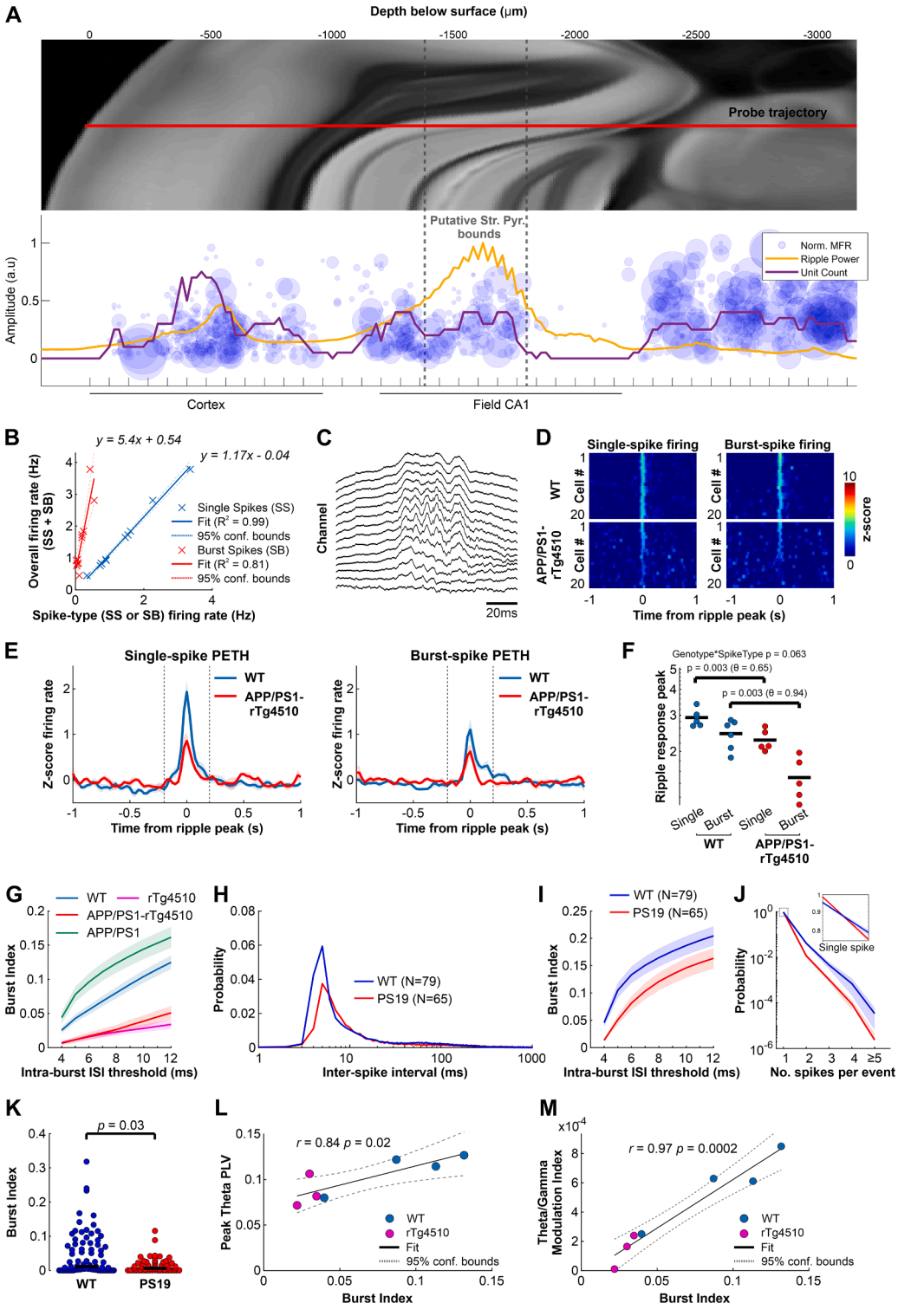

(legend on next page)

Figure S1. *In vivo* Neuropixels recordings to investigate burst spiking in putative excitatory neurons of CA1, related to Figures 1, 2, 3, and STAR Methods

(A) Top: Allen CCF v3 atlas image of estimated probe trajectory (image rotated such that the trajectory is along the horizontal) as a function of depth through cortex and hippocampus CA1. Bottom: unit count (purple trace, a.u.) and ripple band power (110–250 Hz, yellow trace, a.u.) along the probe shank, with each blue bubble denoting the unit template amplitude (y axis, a.u.) and mean firing rate (MFR, radius of bubble, a.u) over the experimental session of an individual unit. Corresponding anatomical labels from Allen CCF atlas given in the abscissa. Dashed gray lines indicate putative bounds for the CA1 pyramidal region centered on the peak of the ripple trace, illustrating close correspondence with anatomical structures.

(B) Linear regression modeling of single or burst spike rates (SS or SB, respectively, *x* axis) versus overall neuronal firing rates (i.e., SS + SB, *y* axis) across genotypes. Solid lines denote fit for each spike type with dashed lines indicating 95% confidence intervals (equations added as insets). Note the elevated goodness-of-fit (R^2) values in both cases and how small increases in burst firing are associated with large increases in overall firing rate. The model describing the relationship between burst spike and overall firing rates was sufficient to closely predict the marked reduction in overall firing rates experimentally observed in APP/PS1-rTg4510 mice relative to WTs (see also Figure 2H).

(C) Example high-frequency ripple event across depths in CA1 with each trace denoting the LFP average across six channels (equivalent to 60 μm depth) and upper and lower traces corresponding to more superficial and deeper layers, respectively.

(D) PETHs of neuronal responses to ripple events, decomposed into single and burst spiking contributions. Heatmaps illustrate *Z* scored firing rates of top 20 responding hippocampal neurons for each genotype and spike type. Note the visible suppression of both single and, to a greater extent, burst spiking during ripples in APP/PS1-rTg4510 neurons.

(E) Averaged PETHs displaying *Z* scored firing rate responses to ripple events across hippocampal neurons within animals/genotypes ($N = 6$ WT, $N = 5$ APP/PS1-rTg4510) for single-spike (left) and burst spike (right) firing. Solid lines are means across animals for each genotype, with shaded areas as SEM.

(F) Quantification of peak firing rate responses to ripple events (maximum *Z* score within ±0.2 s of ripple peak, see dashed lines in E), showing a significant reduction in both single spike and, to a greater degree, burst spike firing in APP/PS1-rTg4510 mice ($N = 5$) versus WTs ($N = 6$). Two-way mixed ANOVA following log transformation, indicating significant interaction between genotype and spike type $F(1,9) = 4.48$, $p = 0.063$ with Tukey-Kramer post hoc comparisons. The mean-difference effect size (Θ, given alongside *p* values) between genotypes was larger for burst spiking (0.94) than single spiking (0.65), indicating a more pronounced debilitation of the former in APP/PS1-rTg4510 animals.

(G) Genotype-specific differences in burst index were qualitatively similar across a range of intra-burst ISI thresholds (4–12 ms) for WT, rTg4510, APP/PS1-rTg4510, and APP/PS1 neurons. Data as means across neurons for each genotype (WT = 167 from 4 mice, rTg4510 = 56 from 3 mice, APP/PS1-rTg4510 = 54 from 3 mice, and APP/PS1 = 98 from 3 mice), with shaded error bars as SEM.

(H) ISI distribution for neurons from tau-overexpressing PS19 mice and WT controls, indicating an attenuated and delayed intra-burst ISI peak (2–6 ms) in PS19 neurons versus controls. Data as means across neurons for each genotype (cell numbers given as inset from $N = 3$ mice per genotype), error bars omitted for clarity.

(I) Burst index for neurons from tau-overexpressing PS19 mice and WT controls over a range of intra-burst ISI thresholds (4–12 ms, as in G), suggesting an overall reduction in burst index in PS19 neurons. Data as means across neurons for each genotype (cell numbers given in inset from $N = 3$ mice per genotype), with shaded error bars as SEM.

(J) The probability of observing single spikes and *n* spikes during a burst event (at an intra-burst ISI threshold of 4 ms) decreased more steeply in PS19 neurons versus WT control neurons, with an increase in the probability of observing single spikes in the former (inset). Data as means across neurons for each genotype (cell numbers as in H), with shaded error bars as SEM.

(K) Burst index at an intra-burst ISI threshold of 4 ms was significantly reduced in PS19 neurons versus WTs. LME model with WT as reference level; fixed effects coefficients: intercept, 0.045 [0.02–0.066, 95% CI], tStat = 4.38, $p < 0.0001$; PS19, −0.03 [−0.06–0.003, 95% CI], tStat = −2.15, $p = 0.033$. Black bars indicate medians, with each datapoint denoting a single neuron, cell numbers as in (H), across three mice per genotype.

(L) Positive correlation (Pearson coefficient and *p* value provided in inset) between theta-PLV peak amplitude and burst index across animals. Solid line indicates linear regression model fit with dashed lines depicting 95% confidence intervals and each marker denoting an individual animal.

(M) Significant positive correlation (Pearson coefficient and *p* value provided in inset) between theta-gamma MI (phase amplitude coupling) and burst index across animals. Solid line indicates linear regression model fit with dashed lines depicting 95% confidence intervals and each marker denoting an individual animal.

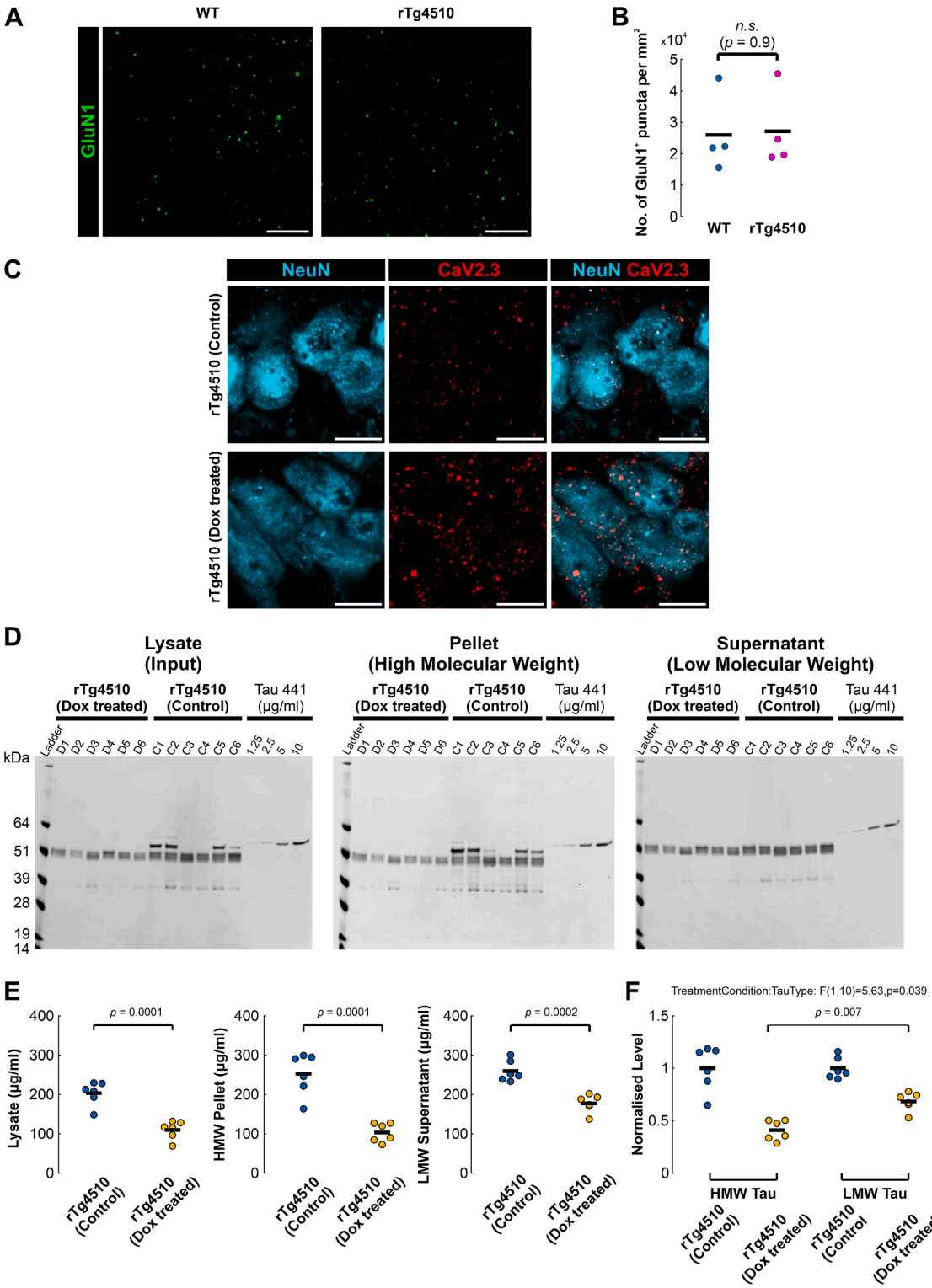

Figure S2. Additional immunohistochemical characterization and tau quantifications by western blot, related to Figure 4

(A) No change in the amount of GluN1 (NR1) in 3-month-old rTg4510 mice. Immunofluorescent images showing GluN1 (green) in the stratum oriens of CA1 of 3-month-old WT (left) and rTg4510 (right) mice. Scale bar, 10 µm.

(B) Quantification of the number of GluN1 (NR1) puncta showing no difference between WT and rTg4510 mice. Each datapoint represents an individual animal (N = 4 per genotype) with black bars denoting means. Unpaired t test: T(6) = 0.14.

(legend continued on next page)

(C) Example immunofluorescence images showing NeuN (cyan) and CaV2.3 (red) in the pyramidal layer of CA1 of a 6-month-old rTg4510 untreated mouse (top) and Dox-treated rTg4510 mouse (bottom). Scale bars, 10 μm.

(D) Total (lysate), HMW (pellet), and LMW (supernatant) tau quantification by western blot in 6-month-old untreated and Dox-treated rTg4510 mice ($N = 6$ for both conditions), using recombinant Tau-441 as a standard curve and probed with HT7 antibody.

(E) Quantification of the western blot signal intensity for all cases, indicating significant reductions in total (lysate), HMW (pellet), and LMW (supernatant) tau in Dox-treated rTg4510 mice versus controls ($N = 6$ per condition, all unpaired t tests: $T(10) = 6.01$, $p = 0.0001$; $T(10) = 6.2$, $p = 9.87e{-}5$, $T(10) = 5.69$, $p = 0.0002$, respectively).

(F) Significant interaction between treatment condition (untreated versus Dox treated) and tau type (HMW versus LMW) and a significantly greater reduction in HMW versus LMW in Dox-treated animals (two-way mixed ANOVA, $F(1,10) = 5.63$, $p = 0.039$, with Tukey-Kramer post hoc tests, data normalized to mean level in untreated rTg4510 controls for each tau species).

A

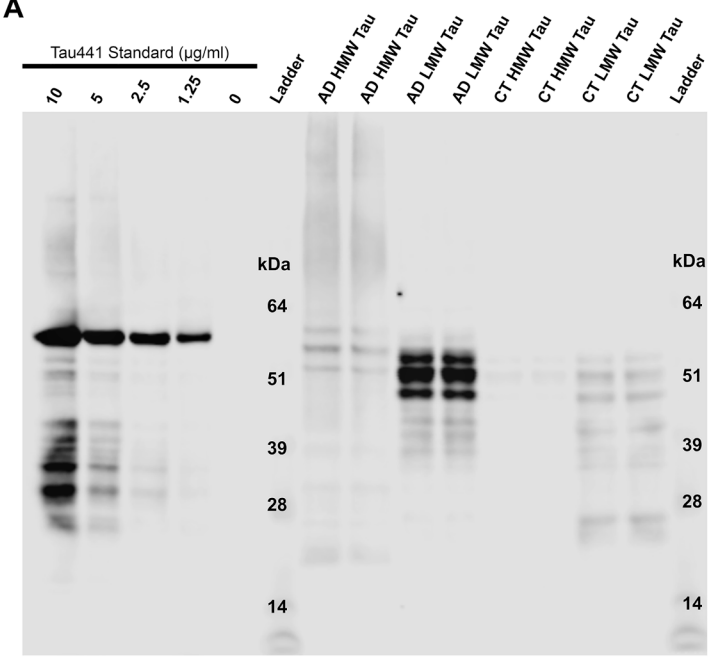

	Concentration from standard curve (µg/ml)
AD HMW	3.66827181
AD HMW	2.356044496
AD LMW	7.326602504
AD LMW	6.899134515
CT HMW	0.088575344
CT HMW	0.076844827
CT LMW	1.670107491
CT LMW	1.560755215

(Averages)	Concentration from standard curve (µg/ml)
AD HMW	3.012158
AD LMW	7.112869
CT HMW	0.08271
CT LMW	1.615431

B

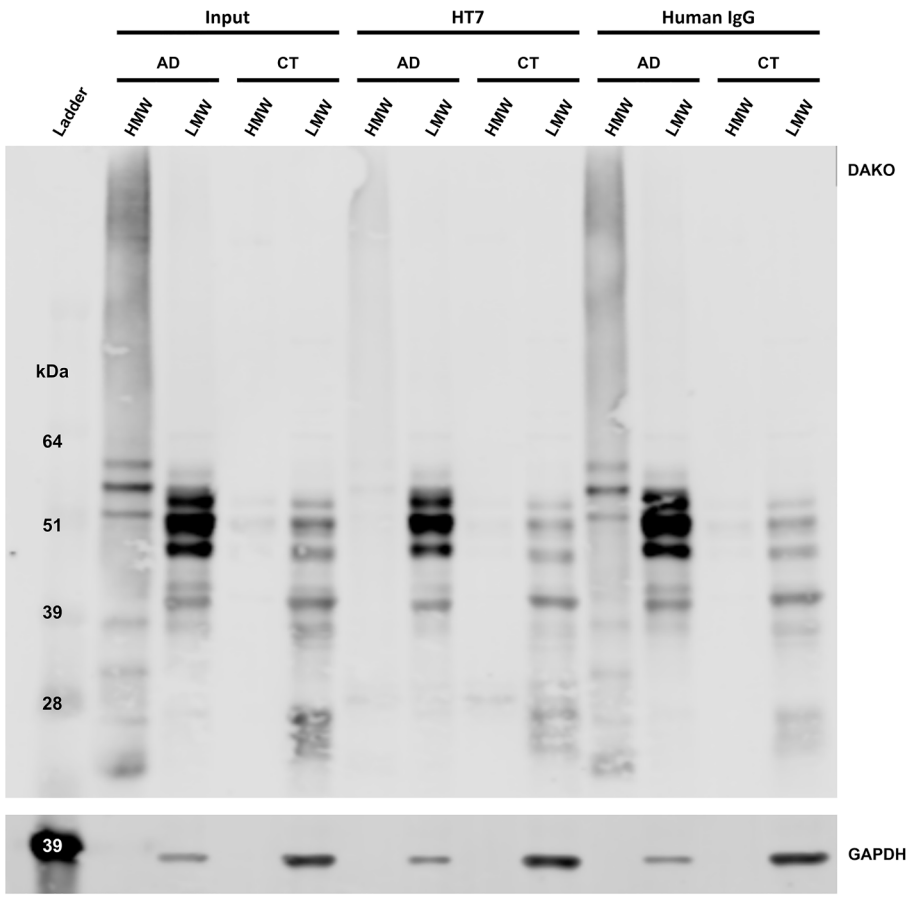

(legend on next page)

Figure S3. Western blots for quantification of HMW and LMW tau concentration in human brain extracts, related to Figure 5

(A) Left, HMW and LMW tau quantification in an AD and healthy control (CT) human brain by western blot, using recombinant Tau-441 as a standard curve, and probed with Dako anti-human tau antibody (Donkey anti-rabbit 680 secondary). Right, quantification of HMW and LMW concentration in each brain using Tau-441 standard curve and western blot signal intensity (final averages given in lower table).

(B) Western blot showing immunodepletion of HMW and LMW tau in AD and CT patient brain samples by HT7 antibody and probed with Dako anti-human tau antibody and anti-GAPDH. GAPDH is present only in LMW tau samples due to its size discrimination by SEC.

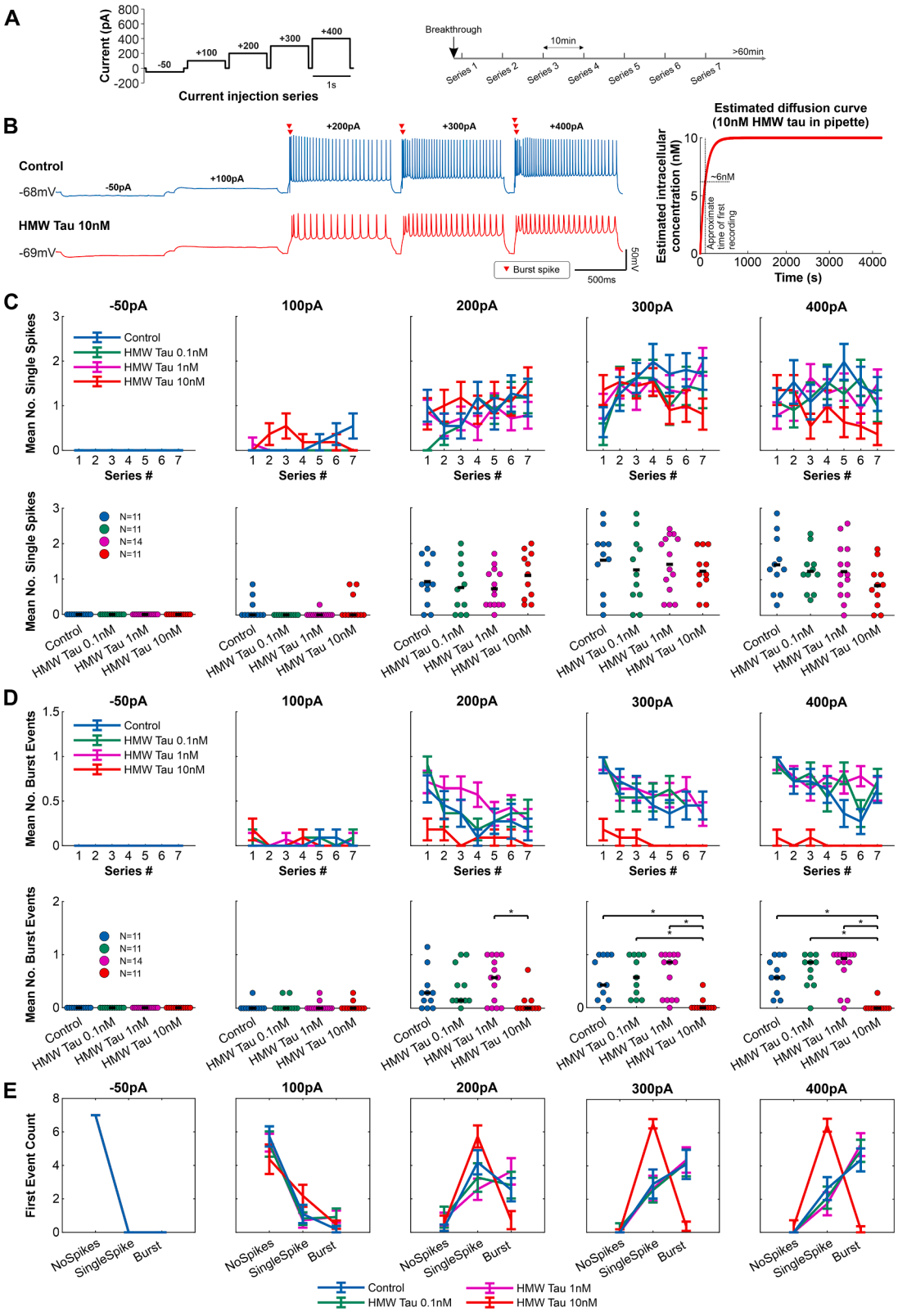

(legend on next page)

Figure S4. Description of *in vitro* patch-clamp recording protocol and further quantifications examining the effect of varying concentrations of HMW tau on neuronal spiking, related to Figure 5 and STAR Methods

(A) Left, schematic showing current injection series comprising 5 current injection steps ranging from −50 to 400 pA. Right, schematic showing that seven current injection series (each containing five increasing current injection steps, as in left) were presented after cell breakthrough (∼120-s delay), with a 10-min interval between series and a total recording time of >60 min.

(B) Left, example *in vitro* voltage traces showing neuronal spiking responses to the first series of five current steps in two patched pyramidal neurons, in which the pipette was pre-loaded with control solution (top) or 10 nM HMW tau (bottom). The control condition pertains to HT7 immunodepleted fraction, prepared using the same solution volume as the 0.1 nM HMW tau condition. Right, estimated diffusion of 10 nM tau from patch pipette into cell body over the entire recording time period (>60 min), showing progressive increase in intracellular tau concentration until reaching a steady state. First recordings were typically performed ∼120 s following cell breakthrough (vertical dashed line), at which point the intracellular tau concentration is estimated to be ∼6 nM (see inset text).

(C and D) Effects of HMW tau concentration, as a function of current step and current injection series, on single spikes (C, quantification in lower panel) and burst events (D, quantification in lower panel). Note the non-linear effects of current step and time/series on neuronal metrics, with the greatest amount of bursting at lower HMW concentrations occurring at the maximum current step of 400 pA. Traces are shown as mean and SEM across cells per condition (N = 11, control; N = 11, 0.1 nM HMW tau; N = 14, 1 nM HMW tau; N = 11, 10 nM HMW tau). Asterisks denote $p < 0.05$ for Tukey-Kramer post hoc comparisons following a significant ANOVA or Kruskal-Wallis test.

(E) Analysis of the first spiking event immediately following current injection step onset, illustrating increased propensity for single spikes, rather than burst events (two or more spikes), at higher current steps in the presence of 10 nM HMW tau.

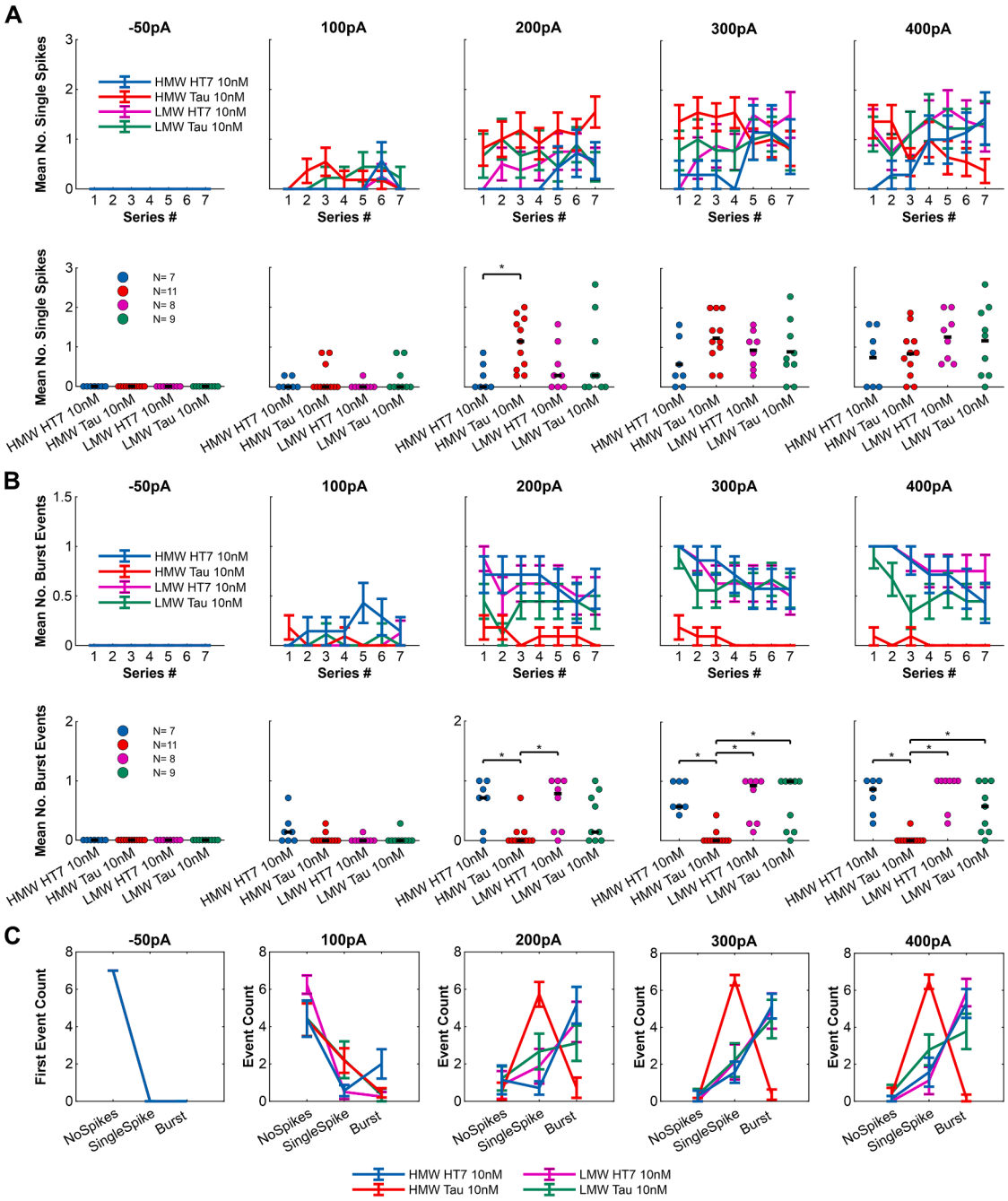

Figure S5. Further quantifications examining effects of 10 nM LMW and 10 nM HMW tau on neuronal spiking across current steps, related to Figure 5

(A and B) Comparison of effects of LMW and HMW tau from the same AD patient extract, and HT7 immunodepleted fractions, as a function of current step and current injection series, on single spikes (A, quantification in lower panel) and burst events (B, quantification in lower panel). Note the selective HMW tau species effect on bursting at higher current injection steps. Traces are as mean ± SEM across cells per condition. Asterisks denote $p < 0.05$ for Tukey-Kramer post hoc comparisons following a significant ANOVA or Kruskal-Wallis test.

(C) Analysis of the first spiking event following current injection step onset, indicating increased propensity for single spikes, rather than burst events (two or more spikes), at higher current steps in the presence of 10 nM HMW tau, relative to LMW and HT7 immunodepleted fractions.

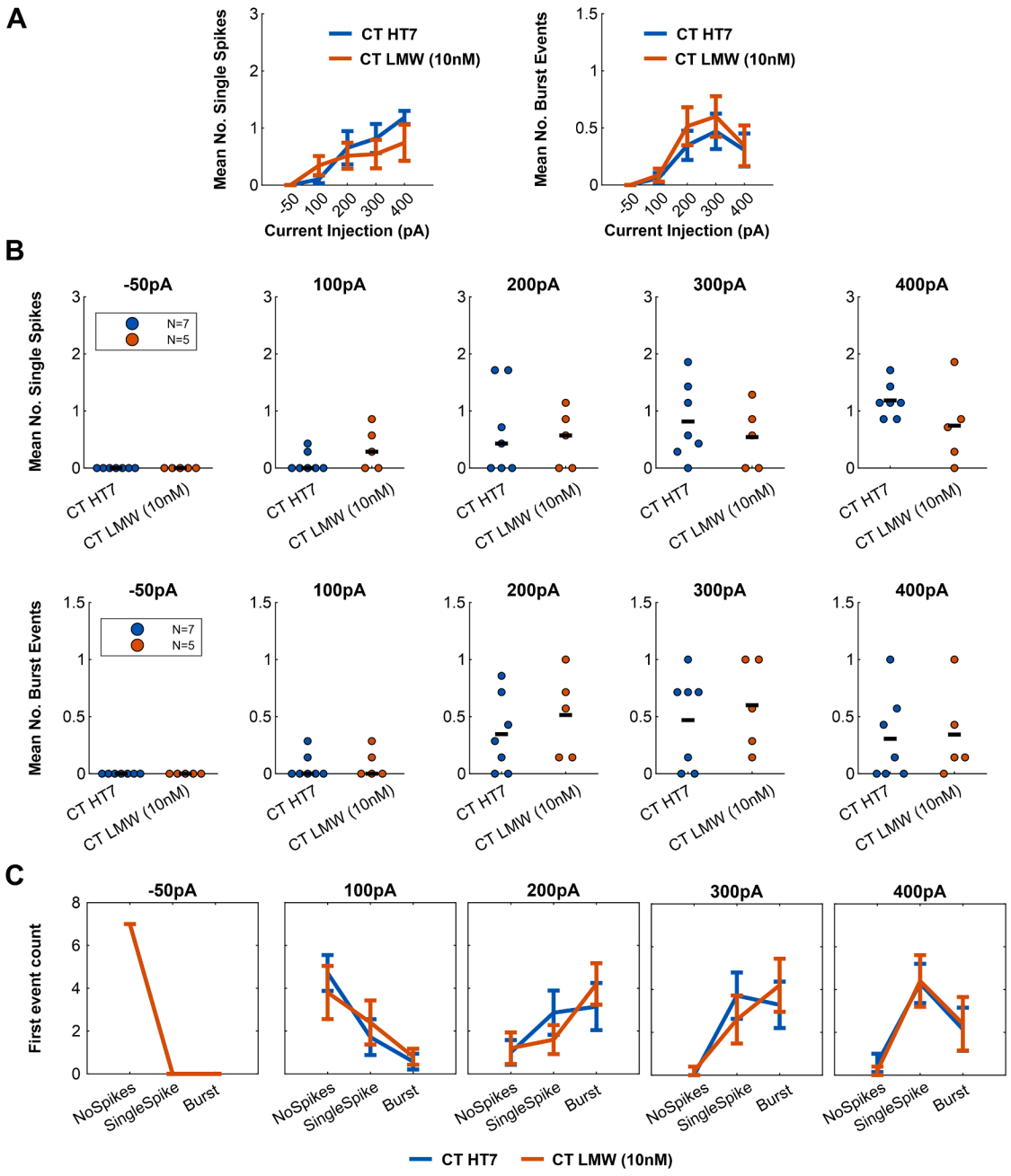

Figure S6. No effect of control patient-derived LMW tau on neuronal bursting, related to Figure 5

(A) No difference in the mean number of single-spike or burst events as a function of current injection (−50–400 pA) in cells infused with control (CT) patient-derived 10 nM LMW tau versus HT7 immunodepleted tau fraction. Data as means across cells (N = 7, CT HT7; N = 5, CT LMW) with error bars as SEM.

(B) Quantifications showing no significant impact ($p > 0.05$ in all cases) of CT 10 nM LMW tau on single-spike or burst generation at each current injection step versus HT7 immunodepleted fraction (CT HT7).

(C) Analysis of the first spiking event immediately following each current injection step onset, illustrating no changes in the propensity for single spikes or burst events (two or more spikes) at varying current steps in the presence of 10 nM LMW tau and relative to immunodepleted fraction.

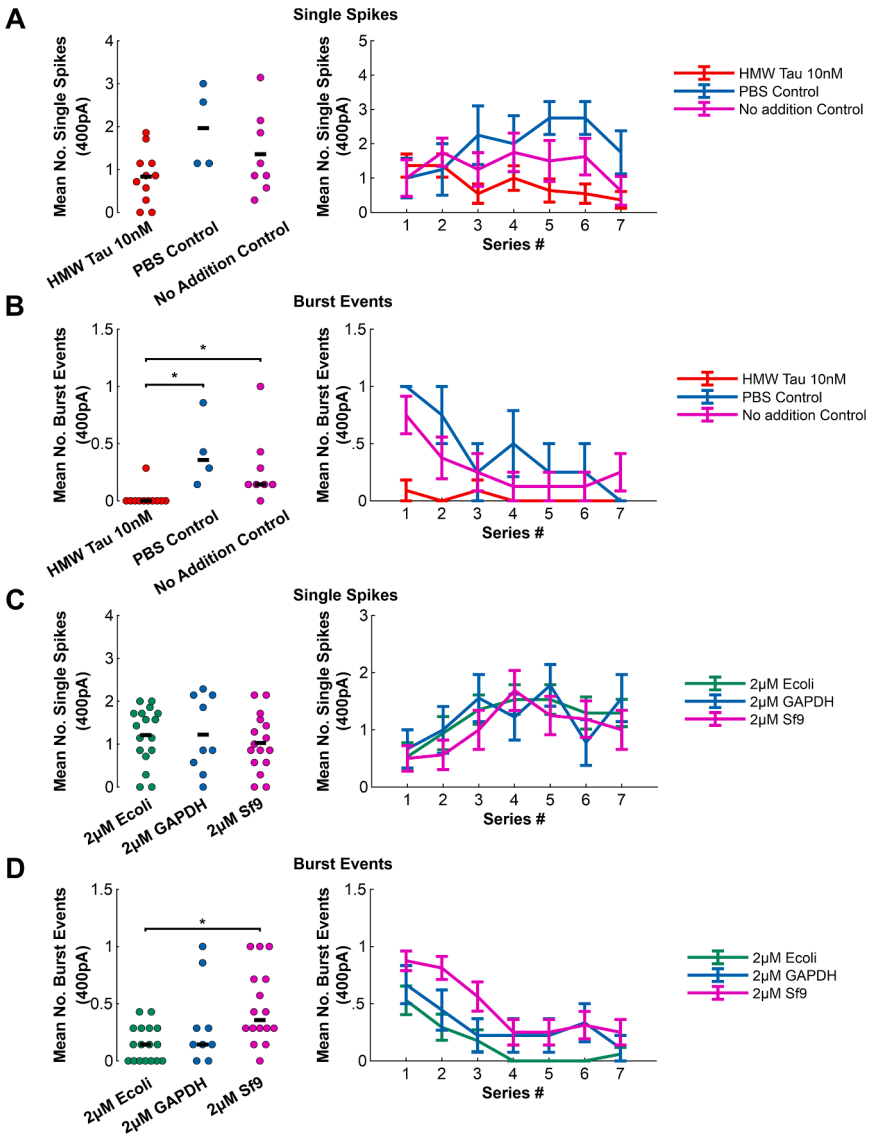

Figure S7. Additional control experiments indicating specific effect of HMW tau (10 nM) on neuronal bursting, related to Figure 5

(A and B) 10 nM HMW tau was associated with a significant reduction in the number of burst events elicited relative to control conditions at 400 pA, in which no addition or PBS alone (at same volume) was added to the standard pipette solution. Quantification in (A), single spikes: one-way ANOVA, $F(2,20) = 3.1$, $p = 0.07$, black bars indicate means; (B) bursting: Kruskal-Wallis test, chi-sq(2) = 13.2, $p = 0.001$, black bars indicate medians. Both tests with Tukey-Kramer post hoc comparisons (asterisks denote $p < 0.05$). Each datapoint denotes an individual cell, $N = 11$ (10 nM HMW tau), $N = 4$ (PBS control), $N = 9$ (no-addition control). Time series as means with errors bars as SEM.

(C and D) No significant reduction in neuronal metrics with recombinant *E. coli*-derived (monomeric, unphosphorylated) or SF9-derived (oligomeric, hyper-phosphorylated) forms of tau versus GAPDH control (all 2-μm concentrations) at 400 pA current step. Quantification in (C), single spikes: one-way ANOVA, $F(2,39) = 0.34$, $p = 0.7$, black bars indicate means; (D) bursting: Kruskal-Wallis test, chi-sq(2) = 9.7, $p = 0.01$, black bars indicate medians. Both tests with Tukey-Kramer post hoc comparisons (asterisks denote $p < 0.05$). Each datapoint denotes an individual cell, $N = 9$ (GAPDH control), $N = 17$ (*E. coli* tau), $N = 16$ (SF9 tau). Time series as means with errors bars as SEM.